M 2026

U.PORTO
FEUP FACULDADE DE ENGENHARIA
UNIVERSIDADE DO PORTO

Solar Power Beyond Earth:
Engineering Flexible Perovskite Solar Cells for Space Applications

FRANCISCO SANTOS
MASTER'S DISSERTATION IN CHEMICAL ENGINEERING
PRESENTED TO THE FACULTY OF ENGINEERING
OF THE UNIVERSITY OF PORTO

Master in Chemical Engineering

Solar Power Beyond Earth: Engineering Flexible Perovskite Solar Cells for Space Applications

Master's Dissertation

of

Francisco Miguel Lima Santos

Developed within the scope of the Dissertation course unit

held in

LEPABE (Laboratory for Process Engineering, Environment, Biotechnology and Energy)

Supervisor at FEUP: **Profª. Luísa Andrade**

Joint supervisor(s) at FEUP: **Doctor Vera Duarte**

FACULTY OF ENGINEERING OF THE UNIVERSITY OF PORTO

DEPARTMENT OF CHEMICAL AND BIOLOGICAL ENGINEERING

July 2026

Acknowledgment

I would like to thank both my supervisors at FEUP, Profª Luísa Andrade and Doctor Vera Duarte for all the support given to me throughout the duration of the work. I would also like to thank all the staff at the UPTEC lab where the work was performed for how they welcomed me, specially Luís Santos and Andrés Soto as they accompanied the beginning of my work, teaching me the basics necessary for it.

Institutional Acknowledgments

This work was supported by national funds through FCT/MECI: project 2023.17945.ICDT with DOI 10.54499/2023.17945.ICDT (https://doi.org/10.54499/2023.17945.ICDT); LEPABE, UID/00511/2025 (https://doi.org/10.54499/UID/00511/2025) and UID/PRR/00511/2025 (https://doi.org/10.54499/UID/PRR/00511/2025); and ALiCE, LA/P/0045/2020 (https://doi.org/10.54499/LA/P/0045/2020).

Abstract

Growing demand for reliable, lightweight power systems for space missions has driven increased interest in perovskite solar cells (PSCs), which offer competitive efficiencies, tunable optoelectronic properties and flexible-substrate compatibility. However, their long-term behaviour under space conditions, characterised by intense UV radiation, ultra-high vacuum, and the absence of atmospheric filtering, remains insufficiently understood, motivating systematic investigation of their degradation mechanisms under space-relevant conditions.

This work investigates flexible inverted p-i-n PSCs with the architecture PEN-ITO/PTAA/Perovskite/PCBM/BCP/Ag, evaluating their predicted AM0 performance and their stability under prolonged UV irradiation (365 nm, up to 768 h) and short-duration high-vacuum exposure (7.5×10^{-5} Pa, up to 8 h). Two perovskite compositions were studied: methylammonium lead iodide ($MAPbI_3$) and the triple-cation mixed-halide formulation $Cs_{0.05}(FA_{0.85}MA_{0.15})_{0.95}Pb(I_{0.85}Br_{0.15})_3$ (CsFAMA). UV effects on individual PSC layers were assessed by UV-VIS spectrophotometry and scanning electron microscopy (SEM), and complete-device performance under UV and vacuum was evaluated through *J-V* characterisation, and electrochemical impedance spectroscopy (EIS) was used to probe the degradation pathways in each device group.

UV-VIS characterisation revealed clear UV-induced optical degradation of the PEN-ITO flexible substrate, PTAA active layer and $MAPbI_3$ absorber, whereas the CsFAMA absorber remained optically stable after 768 h of irradiation, even when the flexible substrate was irradiated without the temporary glass support and therefore without its UV-filtering effect. At the device level, $MAPbI_3$ PSCs suffered catastrophic performance loss, while CsFAMA devices remained functional throughout. EIS analysis indicated that charge carrier recombination is the dominant limitation in CsFAMA devices, while the poorer response of unsupported flexible devices was consistent with mechanically induced damage, possibly ITO microcracking during handling. High-vacuum exposure produced mild degradation of both compositions, although limited sample sizes and exposure times prevent definitive conclusions. Overall, CsFAMA is a substantially more viable absorber than $MAPbI_3$ for space-oriented flexible PSCs, with transport-layer stability and mechanical integrity identified as the main remaining challenges.

Keywords: Flexible Perovskite Solar Cells, Inverted Structure, Space Application, UV Degradation, High-Vacuum Stability

Resumo

A crescente procura de sistemas de geração de energia fiáveis e leves para missões espaciais tem aumentado o interesse em células solares de perovskita (PSCs), que oferecem eficiências de conversão competitivas, propriedades optoelectrónicas ajustáveis e compatibilidade com substratos flexíveis. Contudo, o seu comportamento a longo prazo em condições espaciais, caracterizadas por intensa radiação UV, elevado vácuo e a ausência de filtragem atmosférica, permanece pouco compreendido, motivando o estudo sistemático dos seus mecanismos de degradação em condições relevantes para o espaço.

Este trabalho investiga PSCs flexíveis de arquitetura invertida (PEN-ITO/PTAA/Perovskita/PCBM/BCP/Ag), avaliando o desempenho previsto em AM0 e a estabilidade sob irradiação UV prolongada (365 nm, até 768 h) e exposição de curta duração a alto vácuo (7.5×10^{-5} Pa, até 8 h). Duas composições de perovskita foram estudadas: iodeto de chumbo e metilamónio ($MAPbI_3$) e a composição tri-catiónica $Cs_{0.05}(FA_{0.85}MA_{0.15})_{0.95}Pb(I_{0.85}Br_{0.15})_3$ (CsFAMA). Os efeitos da exposição UV nas camadas individuais das PSCs foram avaliados por espetrofotometria UV-VIS e microscopia eletrónica de varrimento (SEM), e o desempenho de dispositivos completos sob UV e vácuo foi avaliado através de caracterização *J-V*, e a espetroscopia de impedância eletroquímica (EIS) foi utilizada para sondar as vias de degradação em cada grupo de dispositivos.

A caracterização UV-VIS revelou degradação ótica induzida por UV no substrato flexível PEN-ITO, no PTAA e no absorvedor $MAPbI_3$, enquanto o CsFAMA permaneceu opticamente estável após 768 h de irradiação, mesmo na ausência do suporte temporário de vidro e o seu efeito de filtro UV. As PSCs de $MAPbI_3$ sofreram uma perda catastrófica de desempenho, enquanto os dispositivos com CsFAMA mantiveram funcionalidade fotovoltaica ao longo de todo o ensaio. A análise EIS indicou que a recombinação de cargas é a limitação dominante nos dispositivos CsFAMA, enquanto a resposta mais fraca dos dispositivos flexíveis não suportados foi consistente com danos mecânicos, possivelmente microfissuras no ITO durante o manuseamento. A exposição a alto vácuo produziu degradação ligeira em ambas as composições, embora a quantidade reduzida de amostras e a curta duração das exposições impeçam conclusões definitivas. No geral, o CsFAMA é um absorvedor substancialmente mais promissor do que o $MAPbI_3$ para PSCs flexíveis orientadas para o espaço, sendo a estabilidade das camadas transportadoras e a integridade mecânica identificadas como os principais desafios remanescentes.

Declaration

I hereby declare, under word of honour, that this work is original and that all non-original contributions are indicated and due reference is given to the author and source.

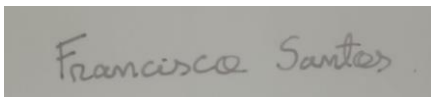

Index

List of Figures

List of Tables

Notation and Glossary[1]

A_0	active area of the device	**cm²**
c	speed of light	**m·s⁻¹**
e	elementary charge	**C**
EQE	external quantum efficiency	**%**
FF	fill factor	
h	Planck constant	**J·s**
I	current	**mA**
J	current density	**mA·cm⁻²**
J_{SC}	short-circuit current density	**mA·cm⁻²**
k^*	AM0/AM1.5 scale factor	
P	power density	**mW·cm⁻²**
P_0	incident power density (photovoltaic characterisation)	**mW·cm⁻²**
PCE	power conversion efficiency	**%**
P_{in}	incident power density	**mW·cm⁻²**
P_{max}	maximum power density	**mW·cm⁻²**
R	reflectance	**%**
R_{rec}	recombination resistance	**Ω**
V	voltage	**V**
V_{OC}	open-circuit voltage	**V**

Greek Letters

λ	wavelength	nm
τ	transmittance	%
Φ	photon flux	photons·s^{-1}·m^{-2}·nm^{-1}

Indexes

*	dimensionless variable
i	index or counter

List of Acronyms

AM0 Air Mass Zero

AM1.5 Air Mass 1.5

BCP Bathocuproine

CsFAMA Caesium Formamidinium Methylammonium

DMF Dimethylformamide

DMSO Dimethyl Sulfoxide

EIS Electrochemical Impedance Spectroscopy

EQE External Quantum Efficiency

ETL Electron Transport Layer

FPSC Flexible Perovskite Solar Cell

HTL Hole Transport Layer

ITO Indium Tin Oxide

$MAPbI_3$ Methylammonium Lead Triiodide

NREL National Renewable Energy Laboratory

PCBM Phenyl-C_{61}-butyric Acid Methyl Ester

PCE Power Conversion Efficiency

PDMS Polydimethylsiloxane

PEN Polyethylene Naphthalate

PET Polyethylene Terephthalate

PSC Perovskite Solar Cell

PTAA Poly(triarylamine)

PV Photovoltaic

SDG Sustainable Development Goal

SEM Scanning Electron Microscopy

UHV Ultra-High Vacuum

UV Ultraviolet

XRD X-ray Diffraction

1. Introduction

1.1. Framing and presentation of the work

The growing global demand for advancements in the space sector has become increasingly evident in the current scientific and political context. Over the past decade, investment from both governments and private sector has significantly increased, reflecting the rising importance of space-based technologies (Figure 1.1) [1]. These technologies have become crucial for communication, Earth observation, and climate monitoring, while their strategic relevance continues to increase, particularly in the context of national security and defence. Concurrently, the sector is undergoing rapid development, driven by private companies such as SpaceX and Blue Origin, which have accelerated technological innovation and reduced access costs [1]. In this context, the development of reliable, lightweight, and high-efficiency power systems has become critical to support long-duration space missions.

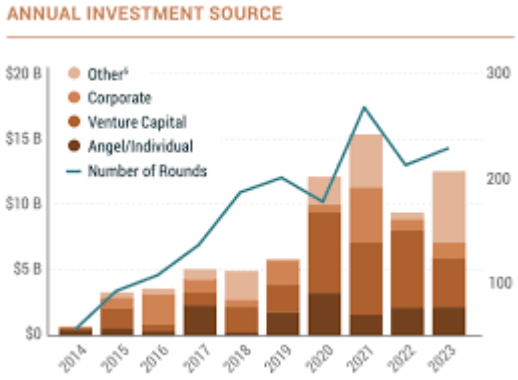

Figure 1.1: Investment in the space technology sector per year [1].

Photovoltaic (PV) technologies remain the primary power source for spacecraft since the first space missions due to their reliability, sustainability, and long operational lifetimes. However, their operation in space presents unique challenges compared to terrestrial environments, including exposure to high-energy radiation, extreme thermal cycling, ultra-high vacuum conditions, and intense ultraviolet (UV) irradiation. Historically, silicon-based solar cells were the dominant technology for space applications [7]; however, their relatively limited radiation resistance and efficiency have led to their gradual replacement by more advanced technologies [7]. Nevertheless, their relatively limited radiation tolerance and lower conversion efficiency compared with III–V technologies have led to their progressive replacement in high-performance space missions by more advanced photovoltaic technologies, particularly multi-junction III–V solar cells. These devices offer superior power conversion efficiency (PCE), excellent radiation tolerance, and long operational lifetimes, making them the current state-of-the-art technology for high-performance space missions. Nonetheless, their widespread adoption is constrained by high manufacturing costs, complex

fabrication processes, and the significant mass and volume associated with conventional GaInP/GaAs/Ge configurations [8]. These limitations have motivated the search for alternative photovoltaic technologies, among which perovskite solar cells (PSCs) have emerged as one of the most promising candidates.

Over the past decade, PSCs have experienced remarkable technological progress, with certified power conversion efficiencies for single-junction devices reaching approximately 27.3% (Figure 1.2) [2], approaching those of the best crystalline silicon solar cells. This rapid improvement is primarily attributed to the exceptional optoelectronic properties of metal-halide perovskites, including tunable bandgaps, high absorption coefficients, long charge-carrier diffusion lengths, and compatibility with low-temperature solution processing techniques [9-10]. These characteristics make PSCs particularly attractive for space applications, where lightweight, flexible, and high-specific-power photovoltaic systems are highly desirable. Their compatibility with flexible substrates enables the fabrication of ultra-lightweight devices with exceptionally high power-to-weight ratios, while their low-temperature processing offers the potential for cost-effective and scalable manufacturing. Furthermore, numerous studies have demonstrated the remarkable tolerance of PSCs to high-energy particle irradiation, reinforcing their potential for operation in the harsh space environment. Despite these advantages, long-term operational stability under combined space stressors - including radiation, thermal cycling, ultraviolet irradiation, and ultra-high vacuum - remains one of the major challenges preventing their widespread adoption in space applications. [9-11].

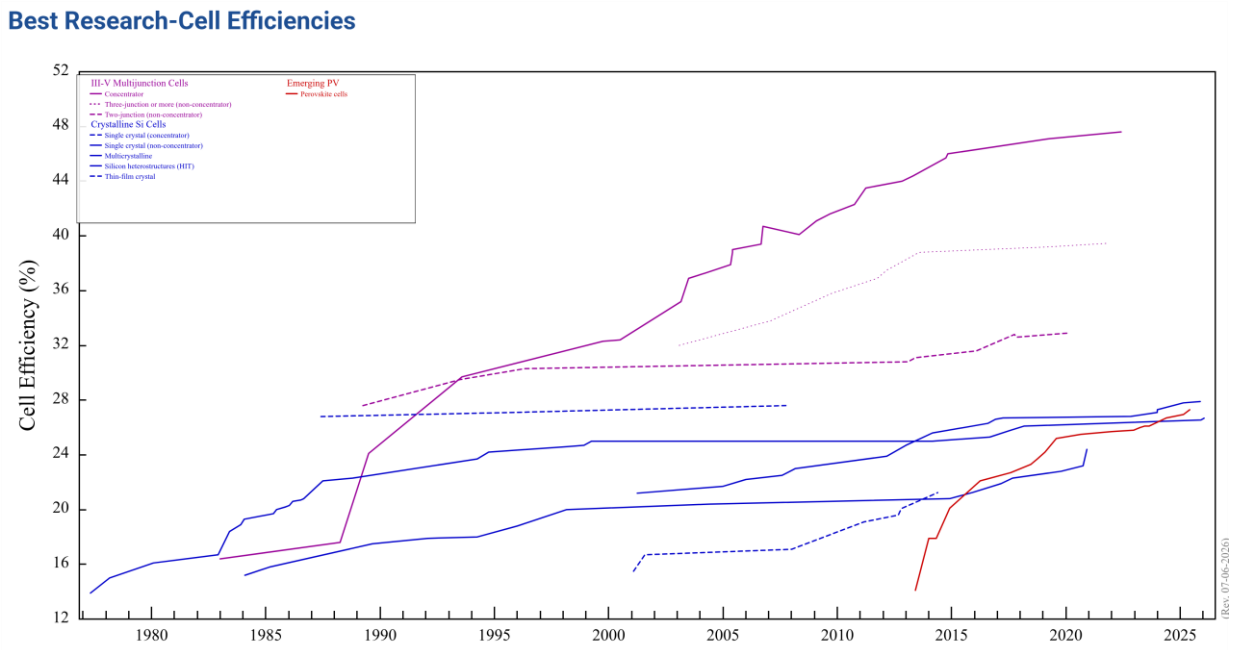

Figure 1.2: Certified best research-cell efficiencies reported for the main photovoltaic technologies as a function of time (1975–2025). Adapted from the NREL Best Research-CellEfficiency Chart. PSCs (red); C-si cells (blue); III-V cells (purple) [2].

To address these challenges, this thesis focuses on flexible inverted perovskite solar cells for space applications. The primary objectives are to investigate the effects of UV degradation on the different layers of PSC devices and evaluate the resulting impact on the device photoelectric parameters over time for two different perovskite absorber compositions and finally the impact of high vacuum degradation on these same device performance metrics. To achieve these objectives, controlled UV and high vacuum exposure experiments, followed by comprehensive optical and electrical characterization of both individual layers and complete devices were performed. Ultimately, this research aims to contribute to the development of space-qualified PSCs by addressing UV and high vacuum induced degradation, critical yet insufficiently understood factors in their practical implementation.

1.2. Contribution of the author to the work

The author's primary contribution to this work was the fabrication of PSCs and the preparation of the different samples used throughout the study. The author also carried out the photovoltaic characterization of the devices, together with their optical characterization by UV–VIS spectrophotometry.

To evaluate the potential performance of the fabricated devices under space operating conditions, the author developed a Python-based computational tool that converts experimentally measured AM1.5 current–voltage (*J-V*) characteristics into their

corresponding AM0 equivalents. This methodology enables the estimation of photovoltaic performance under space illumination using standard terrestrial characterisation equipment.

To investigate the effects of UV irradiation on PSCs and their individual layers, the author designed and assembled a dedicated UV exposure setup inside a glovebox. This experimental configuration enabled controlled UV ageing while minimizing the influence of external environmental factors, thereby allowing the effects of UV irradiation to be studied independently.

To evaluate the influence of ultra-high vacuum on PSC performance, the author used the vacuum conditions available in the laboratory's thermal evaporation system to expose the devices for progressively longer periods. Following each exposure step, the photovoltaic performance of the devices was assessed using the same electrical and optical characterization techniques described above.

1.3. Organization of the dissertation

The present work is organised into seven sections, whose contents are briefly described below. Section 1 introduces the motivation, objectives and scope of the work. Section 2 reviews the current state of the art of PSC technology, with particular emphasis on space applications, relevant absorber compositions and degradation mechanisms under space-relevant conditions. Section 3 describes the materials, device fabrication procedures and characterisation methods employed in this work. Section 4 presents and discusses the experimental results obtained. Section 5 summarises the main conclusions of the work. Section 6 assesses the achievement of the proposed objectives, discusses the contribution of the work to the United Nations Sustainable Development Goals (SDGs), and presents the author's critical reflection on the work developed. Finally, Section 7 lists the references cited throughout the dissertation.

2. Context and State of the Art

Photovoltaic (PV) technologies are commonly classified into three generations: first-generation devices are based primarily on crystalline silicon solar cells (monocrystalline and polycrystalline), second-generation technologies comprise thin-film devices such as chalcogenide-based cells and III-V multijunction solar cells, and third-generation technologies encompass a range of emerging PV concepts [9]. Among the third-generation technologies, PSCs have attracted significant attention and are distinguished by the use of perovskite-structured materials as the light-absorbing layer.

2.1. Perovskite Solar Cells (PSCs)

The term perovskite originally referred to the mineral calcium titanate ($CaTiO_3$), named in honour to the Russian mineralogist L. A. Perovski (1792-1856) [9-10]. Nowadays, the term is used more broadly to describe materials with the general structure ABX_3, where A is a monovalent cation like Cs^+ or $CH_3NH_3^+$, B is a divalent metal (commonly Pb^{2+}) and X is a halide anion like I^-, Br^- or Cl^-. These materials adopt a characteristic corner-sharing octahedral crystal structure, as represented in Figure 2.1.

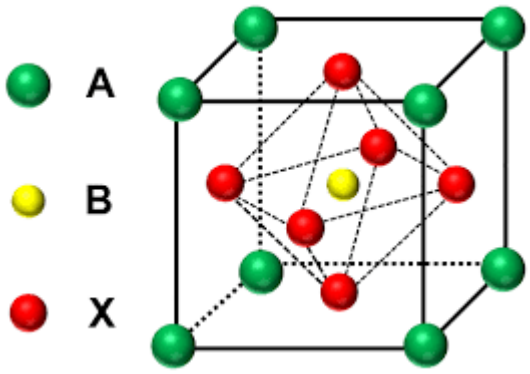

Figure 2.1: Perovskite Crystalline Structure [3].

In PSCs, the perovskite layer acts as a semiconductor absorber, converting the incident photons into electron-hole (e^-h^+) pairs when the photon energy exceeds the material bandgap (E_g). These photogenerated carriers are then separated and transported through adjacent selective contact layers [9]. Efficient charge extraction at the interfaces between perovskite and charge transport layers is therefore essential for high device performance. Perovskite materials exhibit exceptional properties, including high carrier diffusion lengths (>1 μm), high absorption coefficients (>10^5 cm^{-1}), high carrier lifetimes (> 300 ns), and tunable bandgaps. These characteristics make them highly attractive for photovoltaic applications [9-10].

A typical PSC consists of three functional layers: the perovskite absorbing layer, an electron transport layer (ETL), and a hole transport layer (HTL). The ETL and HTL selectively extract

and transport electrons and holes, respectively. These layers are designed to transport their respective charges efficiently to the electrodes and prevent the recombination of e^-h^+ pairs in the perovskite layer. In addition, these layers are usually transparent, enabling efficient light absorption by the perovskite layer. Common HTLs include organic materials like Spiro-OMeTAD, Poly(3,4-ethylenedioxythiophene) (PEDOT) and Poly[bis(4-phenyl)(2,4,6-trimethylphenyl) amine] (PTAA), and inorganic alternatives like NiO_x, CuSCN and CuO_2. Frequently used ETLs include metal oxides like TiO_2, SnO_2 and ZnO and fullerene-based organic materials such as [10]-Phenyl-C61-butyric acid methyl ester (PCBM) [9].

Different device structures have been developed for PSCs, with the most widely adopted being the planar n-i-p (regular) and planar p-i-n (inverted) architectures. In regular structure, light enters through the transparent ETL layer, while in the inverted structure it passes through the HTL layer, as illustrated in Figure 2.2. Another relevant architecture is the mesoporous structure, in which the perovskite infiltrates a porous scaffold (typically an ETL), increasing the interfacial area and enhancing charge separation and transport. This architecture has demonstrated competitive efficiencies; however, the high-temperature fabrication processes limit their application to rigid substrates [9-10].

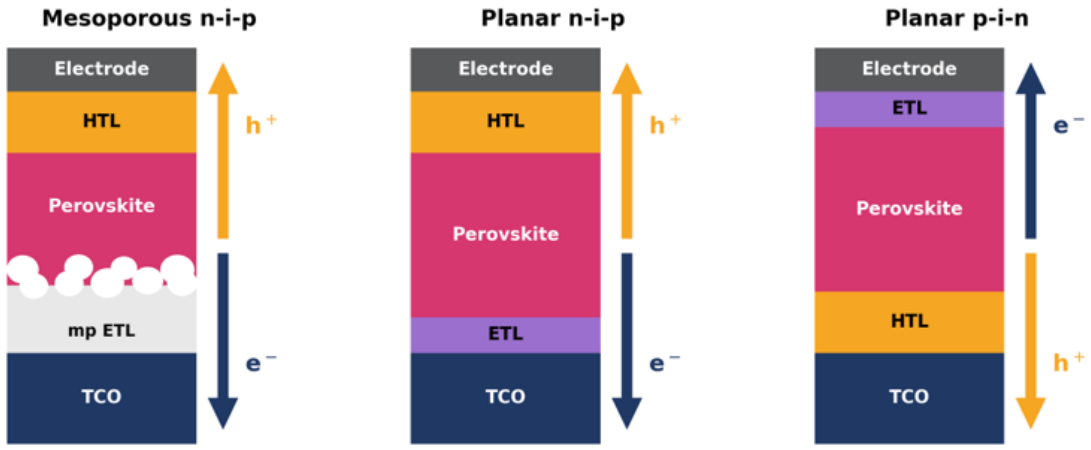

Figure 2.2: Regular, Inverted and Mesoporous Perovskite architecture [4].

Despite their rapid progress, PSCs face critical challenges that hinder their deployment as a dominant technology in the solar energy field. The most significant limitation is their long-term stability. Perovskite materials and associated device layers are highly sensitive to environmental stressors such as moisture, oxygen, temperature, and light exposure. These factors accelerate degradation processes, reducing efficiency and operational lifetime. Consequently, significant research efforts have focused on improving stability through compositional engineering, interface optimization, additive incorporation, and advanced encapsulation strategies [9-11].

2.2. Perovskite Compositions

2.2.1. Methylammonium Lead Triiodide ($MAPbI_3$)

Hybrid Organic-Inorganic Perovskites (HOIPs) contain both organic and inorganic components, unlike fully inorganic perovskites such as $CsPbI_3$. The first PSCs employed HOIP absorbers based on $MAPbX_3$, where X = Cl^-, Br^- or I^-, achieving PCE of approximately 3.8% [12-13]. $MAPbI_3$ has become one of the most extensively investigated perovskite compositions and remains a benchmark material for evaluating new device architectures and fabrication strategies. Its widespread use is attributed to a combination of favorable optoelectronic properties, including a high absorption coefficient *(*1.5×10^4 at 550 nm), long charge-carrier diffusion lengths (>1 μm), and a direct bandgap of 1.57 eV [12-13]. Continuous advances in compositional engineering, crystallisation control, and deposition techniques have substantially improved the performance of $MAPbI_3$-based devices, reaching certified values close to 21.1% by 2019 [14]. Although $MAPbI_3$ exhibits excellent optoelectronic properties, its long-term operational stability remains a challenge. To further improve stability and device performance, mixed-cation and mixed-halide perovskite compositions have been developed, although their stability depends strongly on composition, processing conditions, and operating environment. [11-12].

2.2.2. Triple-Cation Perovskites

One of the most important advances in perovskite compositional engineering has been the development of mixed-cation and mixed-halide structures. The cations used in these structures are generally methylammonium (MA^+), formamidinium ($FA=CH(NH_2)_2^+$]) and cesium (Cs^+), while the halides are typically I^- or Br^-, with small amounts of Cl^- occasionally incorporated.

Mixed-cation compositions reduce the instability associated with MA^+ cation and suppress the phase instability of FA^+, while Cs^+ improves thermal stability and resistance to light-induced degradation [11,15-16]. Although they do not completely eliminate degradation mechanisms, triple-cation perovskites such as $Cs_x(MA_{0,17}FA_{0,83})_{1-x}Pb(I_{0,83}Br_{0,17})_3$ are widely used because of their high efficiency and improved stability [11].

2.3. Perovskite Solar Cells for Space Applications

Solar cells are the primary power source for space applications, providing a reliable and renewable energy supply for long-term missions [7]. Although crystalline silicon (c-Si) solar cells dominated early space applications due to their mature technology, current missions demand higher efficiencies, lower weight, and improved radiation resistance. As a result, multi-junction III–V solar cells have become the state-of-the-art technology, achieving

laboratory PCEs of up to 47.6% while exhibiting excellent stability under high vacuum and ionising radiation [7-8, 17]. However, their fabrication relies on complex and expensive vacuum deposition processes, and their relatively large thickness (>200 μm) limits the specific power to approximately 150-300 $W \cdot kg^{-1}$ [7-8]. Consequently, there is increasing interest in alternative PV technologies capable of reducing launch mass and manufacturing costs.

PSCs have emerged as one of the most promising candidates, with certified PCEs increasing from below 4% to 27.3% within a single decade - a trajectory highly competitive with traditional c-Si performance benchmarks [2]. This unprecedented progress is underpinned by the intrinsic optoelectronic properties of hybrid halide perovskites, already discussed, such as high optical absorption coefficient, long charge-carrier diffusion lengths, excellent carrier mobility, and tunable bandgap. In addition, PSCs require absorber layers typically thinner than 1 μm and can be fabricated through low-temperature solution-processing techniques, enabling lightweight and flexible devices with specific powers between 500 and 1500 $W\ kg^{-1}$, considerably higher than conventional space photovoltaic technologies [7, 18].

Among the different device architectures, inverted (p-i-n) PSCs are considered particularly attractive for space applications. Compared with conventional (n-i-p) structures, they exhibit improved radiation tolerance, reduced current density-voltage (*J-V*) hysteresis, and lower parasitic optical losses [17, 19-21]. Furthermore, the low-temperature fabrication of p-i-n devices is fully compatible with flexible polymer substrates, making this architecture especially suitable for lightweight space photovoltaic systems [19-20].

Flexible PSCs have experienced remarkable progress over the last decade, with efficiencies increasing from 2.62% to over 25%, while maintaining excellent durability after repeated bending cycles [18-19]. Their flexibility enables compact rollable or foldable solar arrays, reducing launch volume and payload mass, which are critical advantages for spacecraft and satellite deployment [8, 17]. Flexible PSCs are generally fabricated on either metallic or polymeric substrates [19]. Metallic foils (e.g., titanium, stainless steel, copper, and nickel) offer excellent electrical conductivity, mechanical robustness, high chemical stability, and superior thermal stability, but require front-side illumination due to their opacity, increasing fabrication complexity [19]. Consequently, transparent polymer substrates such as poly(ethylene terephthalate) (PET) and poly(ethylene naphthalate) (PEN) are preferred because of their low weight, flexibility, optical transparency, and compatibility with roll-to-roll manufacturing [19]. Among them, PEN offers a wider processing window (180–200 °C) than PET (120–150 °C), facilitating the fabrication of high-quality perovskite films.

The transport and electrode materials must also be compatible with low-temperature processing while maintaining mechanical flexibility. In inverted devices, fullerene

derivatives such as PCBM or C_{60} are commonly employed as electron transport layers, whereas PTAA is one of the preferred hole transport materials owing to its excellent photovoltaic performance and radiation tolerance [19]. Indium tin oxide (ITO) remains the most widely used transparent conductive oxide because of its high optical transparency and compatibility with polymer substrates, although its brittleness under repeated bending has motivated the development of alternative transparent electrodes such as indium zinc oxide (IZO) and tungsten-doped indium oxide (IWO) [19].

Despite their outstanding performance, long-term stability remains the main obstacle preventing PSC deployment in space. While the vacuum environment eliminates degradation induced by moisture and atmospheric oxygen, it introduces new challenges. Ultra-high vacuum promotes the outgassing of volatile species, particularly organic cations such as MA^+, potentially altering the perovskite composition. Repeated thermal cycling generates mechanical stresses due to the different thermal expansion coefficients of the device layers, while the intense ultraviolet (UV) component of the AM0 spectrum accelerates interfacial degradation. In addition, continuous exposure to high-energy protons and electrons generates lattice defects that progressively reduce the open-circuit voltage (V_{OC}) and fill factor (FF), despite the partial self-healing capability of halide perovskites [7-8, 16-17]. Overcoming these degradation mechanisms remains one of the major challenges for the successful implementation of PSC technology in future space missions.

2.3.1. Vacuum Degradation in PSCs

Vacuum represents one of the most distinctive stressors affecting PSCs in space applications. Ambient pressure ranges from approximately 10^{-4} to 10^{-10} mbar in Low Earth Orbit (LEO) to below 10^{-10} mbar in Geostationary Orbit (GSO) [17]. Unlike terrestrial environments, where degradation is mainly driven by moisture and oxygen, high vacuum introduces a distinct set of degradation mechanisms, most notably the outgassing of volatile organic components from the perovskite layer and the acceleration of ion migration within the device. The removal of atmospheric pressure eliminates the thermodynamic barrier that normally suppresses these processes, thereby substantially shortening operational lifetimes.

HOIPs are intrinsically soft materials that naturally release volatile organic species under low-pressure conditions. For $MAPbI_3$, the primary decomposition gaseous products include CH_3NH_2, HI, I_2 and NH_3, whereas $FAPbI_3$ additionally releases $HN{=}CHNH_2$ and HCN [20]. The low partial pressure of these species shifts the equilibrium towards perovskite decomposition:

$$\mathrm{MAPbI_3(s) \rightleftharpoons PbI_2(s) + CH_3NH_2(g) + HI\,(g)} \tag{2.1}$$

$$\mathrm{FAPbI_3(s) \rightleftharpoons PbI_2(s) + HN = CHNH_2(g) + HI\,(g) + HCN(g) + NH_3(g)} \tag{2.2}$$

$$PbI_2(s) \rightarrow Pb^0(s) + I_2(s) \quad (2.3)$$

Pressure-dependent studies have shown that decomposition initiates preferentially at grain boundaries under the combined action of illumination and reduced pressure [20]. The volatile gas species generated in reactions (2.1) and (2.2) can either accumulate at the HOIP/HTL interface or escape through the gas-permeable top layers. At pressures close to atmospheric conditions, volatile species remain near the perovskite layer, allowing the reverse reactions to partially restore the crystal structure. As pressure decreases, these species rapidly escape, suppressing the reverse reactions and making degradation irreversible. Cross-sectional scanning electron microscopy (SEM) of devices under progressively lower pressures confirmed that the perovskite layer begins to show pinholes and structural voids at pressures below 2.2×10^4 Pa, with severe morphological transformation and phase segregation at 5×10^3 Pa [20]. Ultra-High Vacuum (UHV) further accelerates light-induced decomposition, increasing the reactions above and promoting the loss of up to 50% of the nitrogen and iodine-containing species [17].

Beyond chemical decomposition of the absorber, vacuum significantly accelerates photo-induced ion migration and accumulation within the device stack. This is intimately linked to defect formation, as the vacancies and interstitial defects created by perovskite degradation serve as migration pathways, particularly for halide hopping. In standard planar architectures, mobile ionic species include cations such as MA^+, FA^+ from the absorber layer, Au^+ from the electrode, as well as halide anions I^- and Br^-. Under illumination, the photo-generated built-in potential drives these species across the device stack, where they accumulate in the charge-transporting layers and interfaces. Their accumulation at transport layers and interfaces increases non-radiative recombination, leading to progressive photovoltaic losses [20].

These degradation mechanisms severely reduce operational lifetime. For single-cation HOIPs, the T80 lifetime (the needed time for PCE to decay to 80% of its original value) decreases from 109 ± 5 h at 9×10^4 Pa to 30 ± 5 h at 2.2×10^4 Pa, and further to 8.5 ± 5 h at 5×10^3 Pa [20]. Importantly, ion migration is not restricted to illuminated devices. Even in dark conditions, high vacuum accelerates halide migration towards the metal electrode, where irreversible degradation products are formed [17]. Consequently, storing PSCs under vacuum without adequate encapsulation may itself induce performance degradation.

The choice of device architecture has been identified as a decisive factor in determining vacuum resilience. Comparative studies have shown that inverted (p-i-n) PSC exhibit substantially higher resistance to UHV exposure than conventional (n-i-p) devices, mainly because ion migration through the hole transport layer is significantly reduced [8]. The

optimised inverted structure ITO/PTAA/Perovskite/PCBM/ZnO/AZO/Ni/Al grid has achieved T_{80} of 4 750 hours, representing almost a 600-fold improvement over a standard planar device. The superior stability was attributed to the elimination of mobile ionic species and the low gas permeability of the compact oxide top contact, both of which are intrinsic characteristics of the inverted configuration [20].

Advanced encapsulation strategies have also been explored to suppress vacuum-induced outgassing and extend device operational lifetime. Hybrid inorganic/polymeric barriers based on Al_2O_3 or SiO_x have demonstrated excellent resistance to volatile outgassing. Specifically, an Al_2O_3/parylene bilayer thin film encapsulant enabled 93% PCE retention after 1000 hours of continuous illumination at 75 °C, while a SiO_x encapsulant system achieved over 90% PCE retention after 3600 hours under combined thermal and vacuum stress (75 °C, 3.07×10^{-4} Pa) [8]. These results demonstrate that long-term operation in space requires a combination of vacuum-stable perovskite compositions, appropriate device architectures and highly efficient encapsulation systems.

2.3.2. UV Degradation in PSCs

Ultraviolet (UV) radiation is one of the most critical degradation factors for perovskite solar cells (PSCs) operating in space. Unlike terrestrial conditions, where part of the UV spectrum is absorbed by the atmosphere, spacecraft are exposed to the Air Mass 0 (AM0) spectrum, which contains a significantly higher UV flux than the AM1.5 spectrum commonly used for terrestrial device characterisation [22]. Some of the resulting damage is metastable and partly recoverable under visible illumination, while other processes are irreversible. Understanding the distinction between these two regimes, while identifying the structural and compositional features that govern resistance to UV exposure, is essential for designing stable PSCs for long-duration space missions.

The most extensively investigated degradation mechanism occurs in conventional (n-i-p) PSC architectures employing TiO_2 as ETL. Under UV irradiation, TiO_2 generates photo-excited electron–hole pairs, and the photogenerated holes oxidise iodide ions (I^-) present at the TiO_2/perovskite interface, producing molecular iodine (I_2) and releasing electrons into the TiO_2 conduction band [22]. This reaction triggers the stoichiometric decomposition of the perovskite absorber:

$$4\mathrm{TiO_2} + 2\mathrm{CH_3NH_3PbI_3} \rightarrow 4\mathrm{TiO_2} - \delta + 2\mathrm{CH_3NH_2} + 2\mathrm{HI} + 2\mathrm{PbI_2} + \mathrm{I_2} \quad (2.4)$$

Lee *et al*. [22] investigated this mechanism systematically by exposing $MAPbI_3$-based solar cells to 365 nm UV light (7.6 $mW \cdot cm^{-2}$) in an inert argon atmosphere at <0.5 ppm humidity, isolating UV as a degradation factor. After 1000 hours of continuous illumination, the PCE dropped to approximately 35% of its initial value, with the fill factor being the most affected

parameter, highlighting an increased interfacial recombination and trap-state accumulation at the TiO_2/perovskite interface. X-Ray Diffraction (XRD) confirmed the progressive conversion of $MAPbI_3$ to PbI_2, consistent with the decomposition reaction shown above. Notably, the short-circuit current density (J_{SC}) exhibited a temporary increase in the early stages of degradation, ascribed to the beneficial passivation of deep-level recombination centres by the newly formed PbI_2 [22]. However, this effect is transient and should not be interpreted as an improvement in device stability.

UV degradation consists of both reversible and irreversible processes. While structural decomposition and PbI_2 formation permanently reduce device performance, UV irradiation also induces ion redistribution and trap-state population, producing metastable losses that can be partially recovered under subsequent one-sun illumination. In contrast, dark storage produces little or no recovery, indicating that visible light promotes the redistribution of mobile ions and the partial restoration of the internal electric field, whereas irreversible chemical decomposition remains unaffected [22].

The coexistence of reversible and irreversible degradation highlights the importance of distinguishing transient performance losses from permanent chemical degradation when assessing PSC stability. Light-dark cycling protocols have therefore been proposed to separate these contributions. For triple-cation perovskites, most of the UV-induced efficiency loss has been shown to be reversible, indicating that ion migration rather than bond breaking dominates the initial degradation process [23]. This interpretation is supported by transient ion-migration measurements, which reveal a significant increase in mobile ion concentration after UV exposure, whereas time-resolved photoluminescence (TRPL) measurements show little variation, suggesting that bulk recombination remains largely unaffected [23]. This suggests that operational tests with rest periods might overestimate PSC stability under UV irradiation. Only continuous tracking of the photoelectric parameter gives us a clear picture of the PSCs' operational lifetime.

Under space conditions, UV radiation acts simultaneously with ultra-high vacuum, producing degradation mechanisms that are more severe than those generated by either stressor individually. At atmospheric pressures, volatile decomposition products are retained near the film surface and can partially recombine with the crystal. In UHV conditions, however, these species are immediately evacuated, making the degradation irreversible and inhibiting the perovskite´s self-healing ability [24]. Yang *et al*. [24] systematically studied this coupled stressor regime by exposing three representative perovskite compositions: $MAPb(I_{0.83}Br_{0.17})_3$, $FA_{0.83}MA_{0.17}Pb(I_{0.83}Br_{0.17})_3$ (FAMA), and $Cs_{0.1}(FA_{0.83}MA_{0.17})_{0.9}Pb(I_{0.83}Br_{0.17})_3$ (CsFAMA), to white-light illumination in UHV conditions, characterising the films before and after exposure. X-Ray Photoelectron Spectroscopy (XPS) measurements focused on the Pb 4f core-level

spectra, where the appearance of a lower binding-energy shoulder is diagnostic of the formation of metallic lead (Pb_0) via photoreduction of Pb^{2+} [Equation (2.5)]:

$$Pb^{2+} + 2e^- \rightarrow Pb_0 \quad (2.5)$$

This reaction produces metallic lead clusters that act as non-radiative recombination centres and provide visible evidence of advanced photochemical decomposition [23]. After 24 hours of white-light exposure in UHV, the ratio of metallic to total lead signal (Pb_0/Pb) was 0.38 for MA, 0.23 for FAMA, and 0.12 for CsFAMA, demonstrating a clear advantage in terms of photostability for CsFAMA [23]. Dark storage in UHV for up to 72 hours, by contrast, produced no detectable change in film composition or crystal structure for any of the three compositions, confirming that light is a necessary co-stressor: vacuum alone did not drive photochemical degradation but irreversibly amplifies the damage initiated by photoexcitation [24]. The enhanced stability has been attributed to the incorporation of Cs^+, which increases lattice rigidity, reduces lattice distortion and promotes the formation of a Cs-rich surface layer that suppresses photocatalytic degradation [24].

Mitigation strategies have focused primarily on suppressing UV-induced photocatalysis. Replacing TiO_2 with UV-stable electron transport materials such as SnO_2 effectively eliminates the photocatalytic degradation pathway while maintaining favourable electronic alignment and low-temperature processability [22]. An alternative approach consists of incorporating luminescent down-shifting (LDS) encapsulation layers, which absorb harmful UV photons and re-emit them within the visible region where they can be efficiently absorbed by the perovskite layer [25]. Combined with photonic light-management structures, these encapsulation systems simultaneously improve UV stability and enhance photocurrent generation, making them particularly attractive for space photovoltaic applications operating under the AM0 spectrum [25].

3. Materials and Methods

3.1. Materials

Indium tin oxide coated polyethylene naphthalate (PEN/ITO) (10^{-15} $\Omega \cdot sq^{-1}$) was purchased from VisionTek Systems Ltd. Polydimethylsiloxane (PDMS) layer was prepared by mixing 10:1 parts of silicone elastomer SYLGARD 184 (DOW) and its curing agent. Poly[bis(4-phenyl)(2,4,6-trimethylphenyl)amine (PTAA) and [10]-phenyl-C_{61}-butyric acid methyl ester (PCBM) were purchased from Ossila. Bathocuproine (BCP) was acquired from Sigma-Aldrich. The 4-fluoro-phenethylammonium iodide compound (F-PEAI) was purchased from TCI Europe N.V. Perovskite films were fabricated using lead iodide (PbI_2) and lead bromide ($PbBr_2$) from TCI Europe N.V., cesium iodide (CsI) from Honeywell, and formamidinium iodide (FAI), methylammonium bromide (MABr) from Greatcell Solar Materials and methylammonium iodide (MAI) from Sigma-Aldrich. Acetone and 2-propanol were purchased from VWR. Anhydrous solvents (2-propanol, chlorobenzene, dimethyl sulfoxide (DMSO), *N*,*N*-dimethylformamide (DMF) and toluene) were purchased from Sigma-Aldrich. Silver (Ag) pellets were purchased from Photon Export.

3.2. Preparation of perovskite solutions

Two perovskite compositions were prepared. The $MAPbI_3$ precursor solution (1.4 M) was obtained by dissolving PbI_2 and MAI in a 1:1 molar ratio in a mixed solvent system consisting of DMF and DMSO in an 8:2 volume ratio. For the triple-cation perovskite, $Cs_{0.05}(FA_{0.85}MA_{0.15})_{0.95}Pb(I_{0.85}Br_{0.15})_3$), PbI_2, $PbBr_2$, MABr and FAI were dissolved in the same DMF: DMSO (8:2 v/v) solvent mixture to obtain a 1.2 M precursor solution. Subsequently, 0.95 mL of the resulting solution was mixed with 0.05 mL of a 1.5 M CsI stock solution in DMSO, yielding the final triple-cation perovskite precursor solution.

3.3. PSC assembly

The PEN-ITO flexible substrates were initially patterned using a 20% HCl solution to selectively remove the ITO layer (etching step). After etching, the substrates were sequentially rinsed with distilled water, acetone, and isopropyl alcohol under sonication. Subsequently, the flexible substrates were attached to rigid glass supports using a polydimethylsiloxane (PDMS) layer applied via spin-coating (4000 rpm; 60s). This step was essential to prevent substrate bending and to enable uniform deposition of the PSC layers during the subsequent processing steps.

All layers of the PSCs were deposited via spin-coating inside a glovebox under an inert atmosphere (N_2). Prior to deposition of the PTAA layer, the substrates were subjected to air plasma treatment for 10 minutes to enhance surface wettability. Subsequently, the PTAA

layer (1.5 mg·mL^{-1} in toluene) was spin-coated onto the substrates (50 µL), followed by thermal annealing at 100 °C for 10 minutes.

After the PTAA deposition, the substrates were treated with argon plasma for 10 seconds to further improve the wettability of the PTAA surface. The perovskite solution described previously in section 3.1 was then prepared. This solution was then spin-coated onto the substrates (60 µL). During deposition, the F-PEAI antisolvent solution (0.125 mg·mL^{-1} in a 9:1 mixture of chlorobenzene and isopropanol) is added (100 µL, 15 seconds before the end of the spin-coating program for both perovskite compositions) to promote crystallization of the perovskite film. The films underwent thermal annealing at 100 °C for 30 minutes.

Following the perovskite layer, a 20 mg·mL^{-1} PCBM solution in chlorobenzene was deposited by spin-coating (50 µL), followed by a thermal treatment step (10 minutes at 100 °C). Finally, a BCP layer (0.5 mg·mL^{-1} in isopropanol, 50 µL) was deposited without any further annealing.

To complete the device fabrication, the cells were mechanically patterned by scraping the side opposite to the etched region. A silver (Ag) back contact (80 nm) was then deposited via thermal evaporation, finalizing the PSC assembly.

3.4. Photovoltaic Characterization

The photovoltaic performance of the fabricated PSCs was evaluated by measuring current–voltage (*I–V*) characteristics using a solar simulator calibrated to the AM1.5 solar spectrum. Masks were used to define the active area of the devices (0.19 cm^2) during measurement. The system consisted of a Zahner electrochemical workstation (Zahner ZENNIUM) connected to a solar simulator (ORIEL LSH-7320 ABA LED Solar Simulator), which was controlled via ThalesXTS.8.3 USB software.

From the measured *I–V* curves, current density–voltage *(J–V)* characteristics were derived. These were used to determine key photovoltaic parameters, namely the open-circuit voltage (V_{OC}), short-circuit current density (J_{SC}), fill factor (*FF*), and power conversion efficiency (PCE). The data methodology for data processing and the corresponding equations are provided in Appendix A.1.

Electrochemical Impedance Spectroscopy (EIS) was carried out on both control and UV-exposed devices to investigate the effects of UV-induced degradation on the different resistive elements of the PSCs.

3.5. AM1.5 to AM0 Conversion

As the photovoltaic characterisation was performed under standard terrestrial AM1.5 illumination, a numerical methodology was developed to estimate the performance of the

fabricated PSCs under the extraterrestrial AM0 spectrum. The AM0 spectrum has a higher total irradiance than AM1.5 (approximately 1360 and 1000 $W \cdot m^{-2}$, respectively) and a different spectral distribution due to the absence of atmospheric absorption and scattering (Figure 3.1).

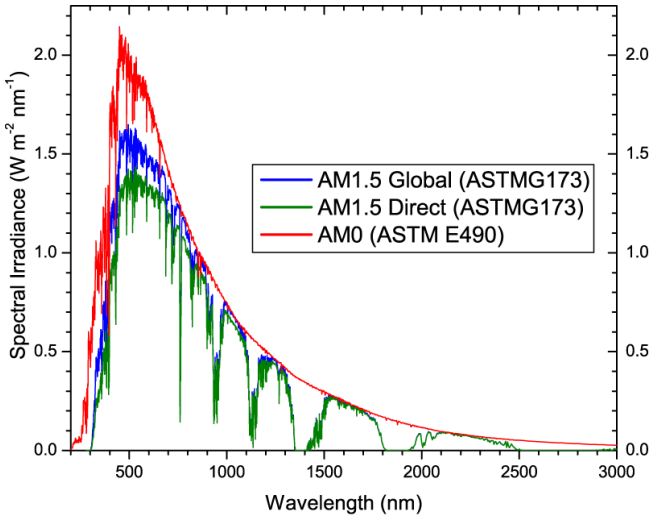

Figure 3.1: AM0 and AM1.5 solar irradiation spectra [5-6].

The conversion methodology is based on the measured external quantum efficiency (EQE) of the solar cells, which describes the wavelength-dependent conversion of incident photons into collected charge carriers. By combining the measured EQE spectrum with the standard AM1.5 and AM0 solar irradiance spectra, the photocurrent generated under each illumination condition can be determined. The difference between the integrated photocurrents was then used to convert the experimentally measured *J–V* curve under AM1.5 illumination into the corresponding curve under AM0 conditions. The EQE for each of the studied compositions was obtained from samples of the respective "dummy cells" produced.

The procedure was automated using a Python script described in Appendix A.3, which imports the experimental *J–V* and *EQE* data together with the standard solar spectra, performs the spectral integration and reconstructs the estimated AM0 J–V curve, from which the main photovoltaic parameters are extracted.

The methodology assumes that the device *EQE* and the electrical characteristics governing the shape of the *J–V* curve remain unchanged between AM1.5 and AM0 illumination, with the spectral correction primarily affecting the photogenerated current. Therefore, the resulting AM0 characteristics should be interpreted as estimates of device performance under the AM0 spectrum rather than as direct experimental measurements under space illumination conditions.

3.6. UV Degradation study

To investigate the degradation effects of UV radiation on PSCs, an experimental setup was assembled inside a glovebox filled with N_2. The setup consisted of an enclosed chamber, in which the devices were placed. A 365 nm UV lamp (2 × 5 W) was positioned at a distance of 8 cm from the devices, as shown in Figure 3.2. The chamber was lined with aluminium foil to prevent external light interference, and a thermostat was installed to monitor and control the internal temperature. The setup was located inside the glovebox to isolate the effects of UV radiation, eliminating the influence of moisture and oxygen, which are key degradation factors for PSCs that are absent in space environments.

Figure 3.2: UV experimental setup.

The effects of UV-induced degradation were evaluated through UV-VIS spectroscopy (UV-VIS-NIR Spectrophotometer, UV-3600i Plus Shimadzu) and *J-V* characterization of the devices, as described in section 3.3. The samples were analysed over time to assess changes in the absorbance of the active layers. Absorbance was determined from the measured transmittance and reflectance values. An example of the Excel worksheet used for these calculations, along with the corresponding equations, is provided in Appendix A.2.

To further quantify the impact of UV degradation on individual layers within the PSC structure, incomplete devices were fabricated and subjected to the same experimental procedure described above. Also, to study the UV filtering effects of the soda-lime glass

support in the device's behaviour, both supported and non-supported $Cs_{0.05}(FA_{0.85}MA_{0.15})_{0.95}Pb(I_{0.85}Br_{0.15})_3$ devices were produced and studied.

In all cases, control devices were stored in the glovebox without exposure to UV radiation in order to isolate the effects of UV and vacuum-induced degradation of the devices.

Scanning Electron Microscopy (SEM) analysis were performed before and after the UV exposure using the Phenom XL desktop.

3.7. High Vacuum Degradation Study

Vacuum exposure experiments were carried out using the vapour deposition system (Oxford Vacuum Science VapourStation 4**)** available in the host laboratory**.** The system is capable to maintaining a stable vacuum level of approximately 750 pbar (7.5×10^{-7} mbar), corresponding to high vacuum conditions. The PSC devices were exposed to these conditions for periods of 3, 6 and 8 hours. To evaluate the effects of vacuum exposure, the devices were characterized both before and after each exposure interval using the procedures described in Section 3.4.

4. Results and discussion

This chapter presents the experimental results obtained throughout this work and discusses their implications for the application of flexible inverted PSCs in space environments. The chapter is organised into four complementary studies. The first evaluates the expected photovoltaic performance of the fabricated devices under Air Mass Zero (AM0) illumination by applying the conversion methodology described in Chapter 3 to the experimentally measured AM1.5 *J–V* characteristics. The second study examines the effect of UV radiation on the optical properties of the individual PSC layers using UV-VIS spectrophotometry. The third study assesses the impact of prolonged UV exposure on the photovoltaic performance parameters of complete PSC devices. The fourth study investigates the effect of vacuum exposure on these same device photovoltaic parameters.

Unless otherwise stated, all devices analysed in this chapter employ an inverted (p–i–n) architecture consisting of PEN-ITO / PTAA / Perovskite / PCBM / BCP / Ag, on flexible PEN-ITO substrates. Two perovskite absorber compositions were investigated throughout the study: methylammonium lead iodide ($MAPbI_3$) and the triple-cation mixed-halide composition $Cs_{0.05}(FA_{0.85}MA_{0.15})_{0.95}Pb(I_{0.85}Br_{0.15})_3$), hereafter referred to as CsFAMA**.** The choice of these two compositions enables a direct comparison between $MAPbI_3$, a single cation perovskite absorber which has been thoroughly researched and can be used as a baseline, and a compositionally engineered mixed-cation system expected to exhibit superior stability under environmental stress, as suggested by the literature [23].

4.1. AM1.5 to AM0 Performance Prediction

To evaluate the potential performance of the fabricated PSCs under space operating conditions, the conversion methodology described in Section 3.5 was applied to the experimentally measured *J–V* characteristics obtained under AM1.5 illumination. The resulting *J–V* curve predicted for the AM0 spectrum is presented in Figure 4.1.

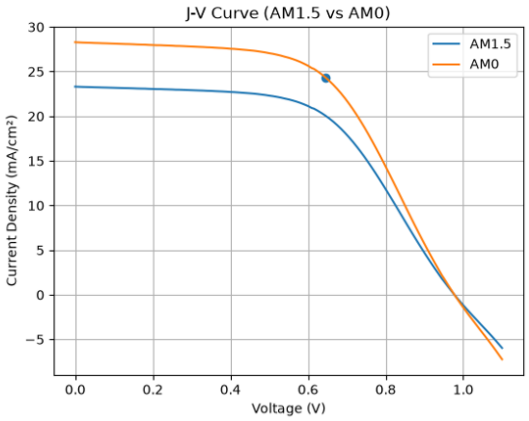

Figure 4.1: Experimental J-V curve measured under AM1.5 illumination and the corresponding curve predicted under AM0 conditions using the developed conversion methodology.

As expected, the transition from the AM1.5 to the AM0 spectrum results in an increase in the generated photocurrent across the entire voltage range. This behaviour is mainly attributed to the higher irradiance of the AM0 spectrum (1360 $W \cdot m^{-2}$ compared with 1000 $W \cdot m^{-2}$ for AM1.5), together with its higher photon flux in the ultraviolet and visible spectral regions, where the device exhibits significant external quantum efficiency. The increase in photocurrent is particularly evident in the short-circuit region, where the predicted current density rises from approximately 23.4 $mA \cdot cm^{-2}$ under AM1.5 illumination to 28.4 $mA \cdot cm^{-2}$ under AM0 conditions, corresponding to an increase of approximately 21%. This variation closely follows the difference in the integrated photon flux between both spectra weighted by the device EQE, confirming the physical consistency of the conversion methodology. In contrast, the open-circuit voltage exhibits only a modest increase, as expected from its logarithmic dependence on the photocurrent. Consequently, the shape of the *J–V* curve remains largely unchanged, with the principal effect being an upward displacement of the current density a corresponding increase in the maximum output power. This behaviour is particularly advantageous for space applications, where the primary objective is to maximise the electrical power delivered by the photovoltaic system under the AM0 solar spectrum. Similarly, only minor variations are observed in the fill factor, indicating that the conversion methodology primarily affects the photogenerated current while preserving the electrical characteristics of the device. This behaviour is consistent with the assumptions adopted by the model (Appendix A.3), namely that the spectral response of the solar cell remains unchanged and that the difference between AM1.5 and AM0 illumination is predominantly associated with the spectral distribution and intensity of the incident radiation.

As a conclusion, the predicted AM0 characteristics indicate that fabricated PSCs would benefit from the increased photon flux available under extraterrestrial illumination, leading to higher photocurrent generation and higher maximum output power. The developed

methodology therefore provides a practical approach for estimating the photovoltaic performance of PSCs under AM0 conditions using conventional AM1.5 photovoltaic characterisation.

4.2. UV Degradation of Flexible Inverted PSCs

4.2.1. UV Degradation of individual layers

To identify the origin of UV-induced degradation within the inverted PSC architecture, a series of dummy cells were fabricated with increasing stack complexity, from the bare glass substrate to the complete device stack excluding the Ag back contact. All samples were exposed to continuous 365 nm UV irradiation inside an inert nitrogen-atmosphere glovebox, as described in section 3, thereby eliminating moisture and oxygen as degradation factors and allowing the effects of UV radiation alone to be investigated. UV–VIS absorbance spectra were recorded prior to exposure (0 h), after 168 h, and after 768 h of continuous UV illumination. For the perovskite-containing dummy cells, both $MAPbI_3$ and CsFAMA compositions were fabricated and studied under identical conditions, enabling a direct comparison. Additionally, one complete CsFAMA dummy cell was fabricated without the supporting glass substrate to evaluate the influence of the glass on UV shielding under conditions more representative of flexible space photovoltaics. Selected samples were further analysed by SEM after UV exposure to correlate optical changes with morphological degradation.

The optical response of the soda-lime glass substrate, PEN-ITO substrate and PTAA layer is presented in Figures 4.2–4.4. Unless otherwise stated, only minor differences were observed after 168 h of UV exposure, whereas the most significant changes occurred after 768 h.

The soda-lime glass substrate exhibits a gradual increase in absorbance, particularly between 400 nm and 800 nm, as can be observed in Figure 4.2. While soda-lime glass is generally considered an inert structural material, its amorphous silica networks contain trace quantities of metal impurities (Fe^{2+}/Fe^{3+} and Mn^{2+}/Mn^{3+}). Under UV radiation below 400 nm these can be ionised and trapped in defects in the silica network creating “colour centres” and new absorption bands in the glass. This is a phenomenon known as UV-induced solarisation [26]. As a consequence, the UV transmittance of the glass progressively decreases during exposure, implying that the effective UV dose reaching the underlying layers is not constant throughout the experiment.

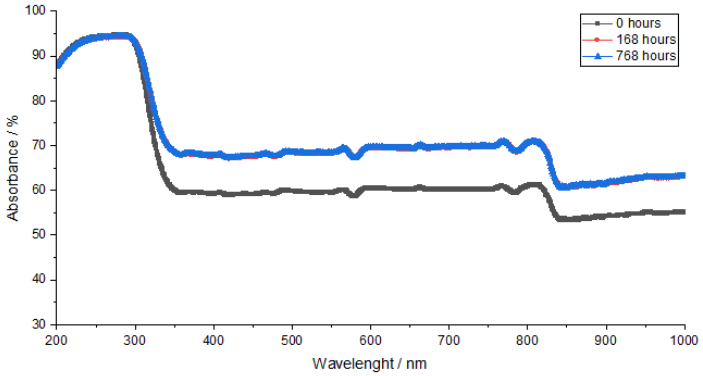

Figure 4.2: UV-VIS absorbance spectra of the soda-lime glass substrate after various levels of UV exposure.

This trend is not observed for the PEN-ITO flexible substrate (Figure 4.3), with the absorbance remaining stable throughout the 768 hour UV ageing. ITO is not expected to undergo significant photochemical degradation under these conditions, but in the absence of oxygen, PEN degradation can occur through direct photolysis [27]. The absence of this effect might have resulted from the chosen exposure interval. This result is particularly relevant for flexible PSCs intended for space applications, where polymer substrates are directly exposed to the higher UV flux associated with the AM0 spectrum.

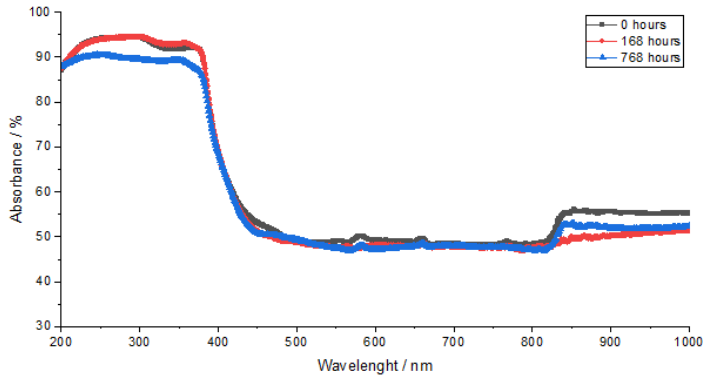

Figure 4.3: UV-VIS absorbance spectra of the PEN-ITO substrate after various levels of UV exposure.

The addition of the PTAA hole transport layer (Figure 4.4) does not significantly alter the overall behaviour of the stack. The absorbance remains essentially unchanged after 69 h but increases noticeably after 768 h, indicating that PTAA also undergoes gradual photochemical degradation under UV irradiation [28]. Under 365 nm radiation, the aromatic amine groups undergo photochemical degradation even in the absence of oxygen, driven by direct absorption of incident photons. Besides modifying its optical properties, PTAA degradation is expected to affect its electronic properties, potentially reducing hole extraction efficiency and altering the built-in electric field at the perovskite/HTL interface [28]. The photochemical degradation of PTAA under UV exposure has also been shown to diminish its absorption of UV radiation leaving the resulting layers exposed to larger doses of that

radiation [28]. These effects are expected to contribute to subsequent losses in the photovoltaic performance of complete devices.

Indeed, these results demonstrate that degradation begins before the perovskite absorber is reached. Both the substrate and the organic hole transport layer undergo gradual photochemical degradation during prolonged UV exposure, while the progressive solarisation of the glass substrate continuously modifies the UV dose reaching the active layers.

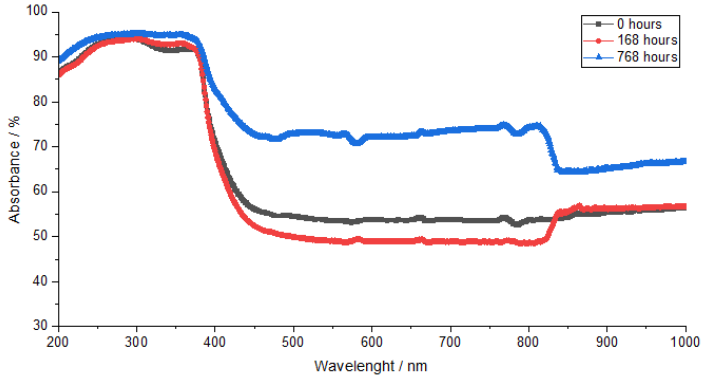

Figure 4.4: UV-VIS absorbance spectra of the PTAA active layer after various levels of UV exposure.

The perovskite absorber is the most critical component of the PSC stack, as its degradation directly affects the photovoltaic performance of the device. To evaluate the intrinsic photostability of the absorber independently of the complete device architecture, dummy cells containing either $MAPbI_3$ or CsFAMA were exposed to prolonged 365 nm UV irradiation under an inert nitrogen atmosphere. The corresponding UV–VIS absorbance spectra are presented in Figures 4.6 and 4.7.

A clear difference in UV stability is observed between the two perovskite compositions. For the CsFAMA absorber exhibits remarkable optical stability throughout the 768 h exposure period, with virtually no changes in either the broadband visible absorption or the absorption edge located at approximately 760 nm (Figure 4.6). These results indicate that prolonged UV irradiation alone does not induce measurable photochemical degradation of the CsFAMA absorber under oxygen- and moisture-free conditions.

In contrast, the $MAPbI_3$ absorber undergoes pronounced degradation after prolonged UV exposure (Figure 4.7). While the absorbance spectrum remains essentially unchanged after 69 h, a significant reduction in absorbance is observed after 768 h, particularly between 500 and 800 nm. This decrease is accompanied by a distinct colour change within the irradiated area of the dummy cell, where the characteristic dark-brown colour of $MAPbI_3$ is replaced by the yellow colour of PbI_2 (Figure 4.5). Since the yellowing is strictly confined to the masked irradiation area, the observed degradation can be directly attributed to UV exposure.

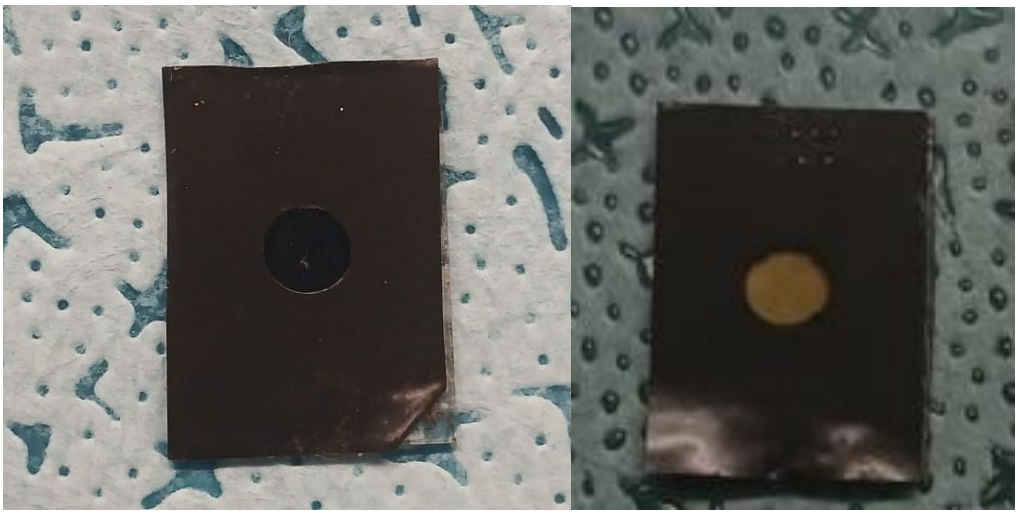

Figure 4.5: $MAPbI_3$ cell before (left) and after (right) the 583 hour UV-exposure period.

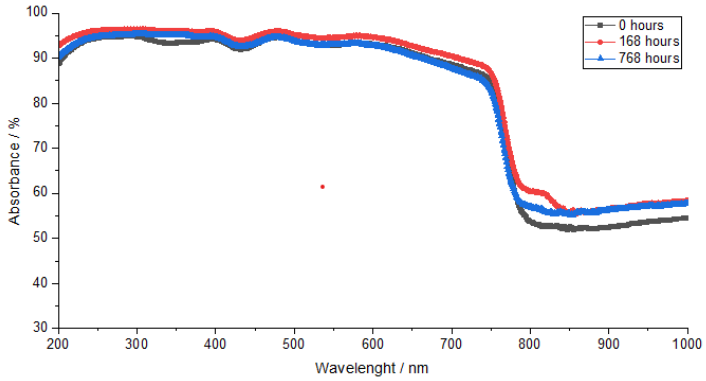

Figure 4.6: UV-VIS absorbance spectra of the supported CsFAMA absorber layer after various levels of UV exposure.

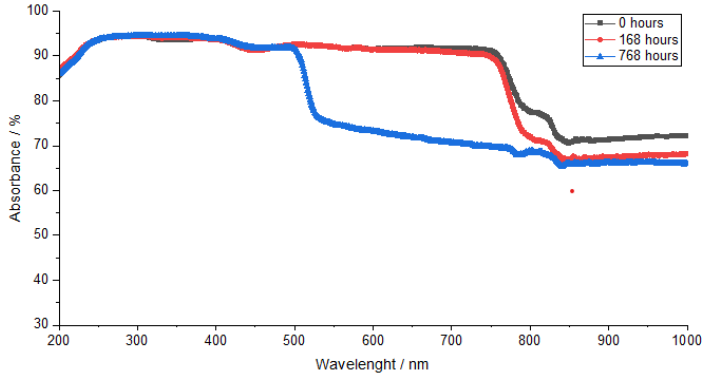

Figure 4.7: UV-VIS absorbance spectra of the $MAPbI_3$ absorber layer after various levels of UV exposure.

The volatile organic decomposition products, methylamine and hydrogen iodide, escape from the film, leaving behind the yellow PbI_2 phase. The fact that the yellowing was confined precisely to the masked irradiation area, with the surrounding regions retaining their original appearance, establishes a clear causal link between UV exposure and the observed

decomposition. Beyond that, this degradation occurred in an inverted p-i-n device stack that does not incorporate a TiO_2 ETL, demonstrating that $MAPbI_3$ photodecomposition under UV is an intrinsic property of the absorber material itself and is not exclusively dependent on the photocatalytic activity of TiO_2 as reported in the literature [22]. The superior photostability of CsFAMA relative to $MAPbI_3$ is consistent with previous reports by Yang *et al.* [23], who demonstrated that mixed-cation perovskite compositions incorporating cesium exhibit significantly lower rates of photoinduced metallic lead formation under white-light illumination in ultra-high vacuum. The incorporation of cesium ions into the A-site of the perovskite lattice reduces the lattice parameter, increases structural rigidity, and promotes the segregation of a Cs-rich passivation layer at the film surface that kinetically suppresses the initiation of photochemical decomposition [23]. Although the present experiments were performed under inert nitrogen atmosphere rather than ultra-high vacuum, the results suggest that these stabilisation mechanisms also provide improved resistance against prolonged UV irradiation.

The UV–VIS results are further supported by the SEM observations of the $MAPbI_3$ dummy cells (Figure 4.8). Before UV-exposure SEM image reveals the characteristic polycrystalline grain morphology of the $MAPbI_3$ film, with clearly defined grains and grain boundaries. After 768 h of irradiation, the surface undergoes substantial morphological degradation, characterised by disruption of the grain structure, the formation of large voids and an overall increase in surface roughness. These changes are consistent with the decomposition of the absorber layer and the formation of lead iodide, which occupies a smaller molar volume than the original perovskite phase. As the volatile decomposition products escape from the film, the crystalline structural integrity of the perovskite is lost, grain boundaries collapse, and the resulting contraction generates the observed voids and surface disruption. The excellent agreement between the optical, visual and morphological observations provides strong evidence that the degradation of $MAPbI_3$ under prolonged UV irradiation is irreversible and originates from intrinsic decomposition of the absorber material.

Concluding, these results demonstrate that compositional engineering plays a decisive role in improving the UV stability of perovskite absorbers. While $MAPbI_3$ undergoes extensive photochemical degradation after prolonged UV exposure, the CsFAMA composition preserves both its optical properties and structural integrity, highlighting the advantages of mixed-cation perovskites for space photovoltaic applications.

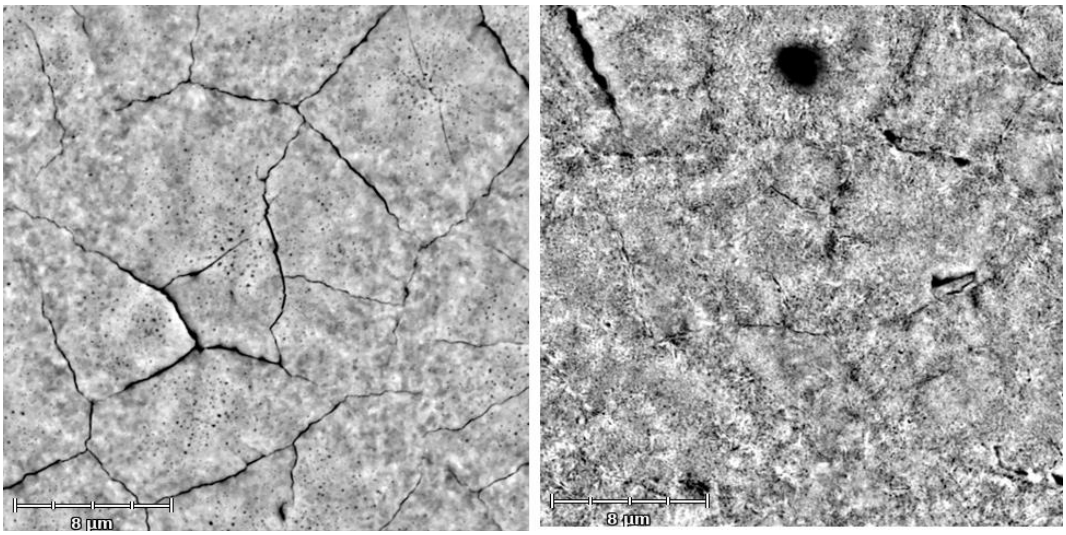

Figure 4.8: SEM images of the $MAPbI_3$ dummy cell before and after 768 h of UV exposure.

The incorporation of the PCBM electron transport layer and the BCP buffer layer modify the degradation behaviour observed for the perovskite-only dummy cells. The corresponding UV–VIS absorbance spectra are presented in Figures 4.9 and 4.10. For the CsFAMA complete stack (Figure 4.9) the optical response remains essentially unchanged throughout the 768 h UV exposure period, with only a slight reduction in absorbance at wavelengths above 800 nm. These results indicate that the addition of PCBM and BCP does not compromise the excellent intrinsic UV stability of the CsFAMA absorber. A more pronounced effect is observed for the $MAPbI_3$ stack (Figure 4.10). Compared with the perovskite-only dummy cells (Figure 4.7), the complete stack exhibits significantly improved optical stability, with only minor changes in the absorbance spectrum after prolonged UV exposure. Nevertheless, visual inspection of the irradiated area still reveals slight yellowing, indicating that partial conversion of $MAPbI_3$ into PbI_2 continues to occur despite the presence of the overlying layers.

The improved stability can be attributed to the passivation effect of the PCBM overlayer. Lin *et al.* [29] demonstrated that a pinhole-free PCBM layer deposited on inverted $MAPbI_3$ devices substantially delays UV-induced optical bleaching by passivating iodide-vacancy defects at the perovskite surface. Since the present experiments were performed under an inert nitrogen atmosphere, the surface passivation mechanism is expected to be the dominant contribution, whereas oxygen-related degradation pathways are absent. This explains why the protection provided by PCBM is significant but not complete.

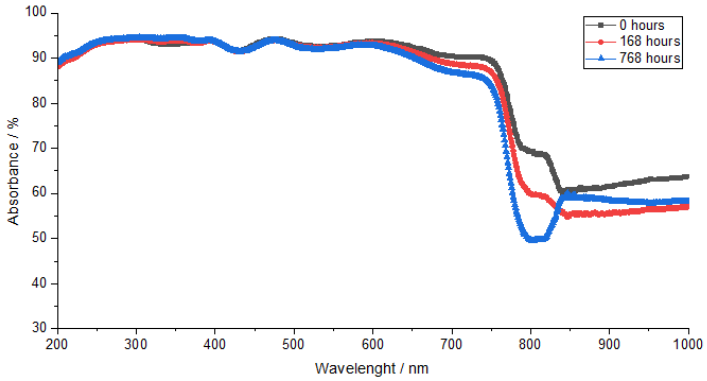

Figure 4.9: UV-VIS absorbance spectra of the supported CsFAMA full stack after various levels of UV exposure.

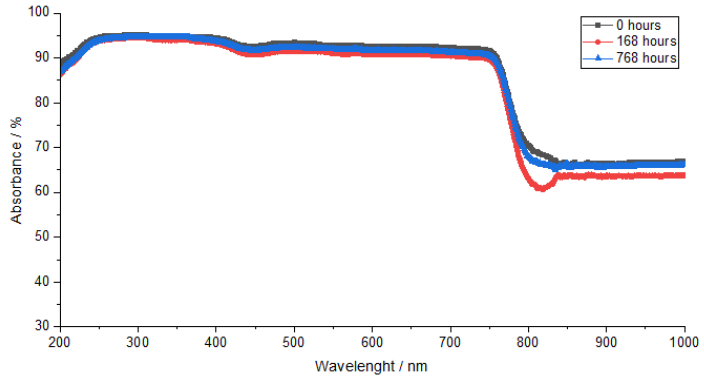

Figure 4.10: UV-VIS absorbance spectra of the $MAPbI_3$ full stack after various levels of UV exposure.

The SEM images for the $MAPbI_3$ complete stack (Figure 4.11) support the fact that the PCBM and BCP overlayers partially preserve the underlying morphology relative to the bare perovskite sample. The after-exposure SEM image shows a somewhat less severe degree of structural disruption, consistent with the partial protective role of these overlayers suggested by the UV-VIS data.

Concluding, these results demonstrate that interface engineering can significantly delay UV degradation of $MAPbI_3$-based inverted PSCs. However, the intrinsic photostability of the absorber remains the dominant factor governing long-term stability, as evidenced by the superior performance of the CsFAMA composition irrespective of the presence of the protective overlayers.

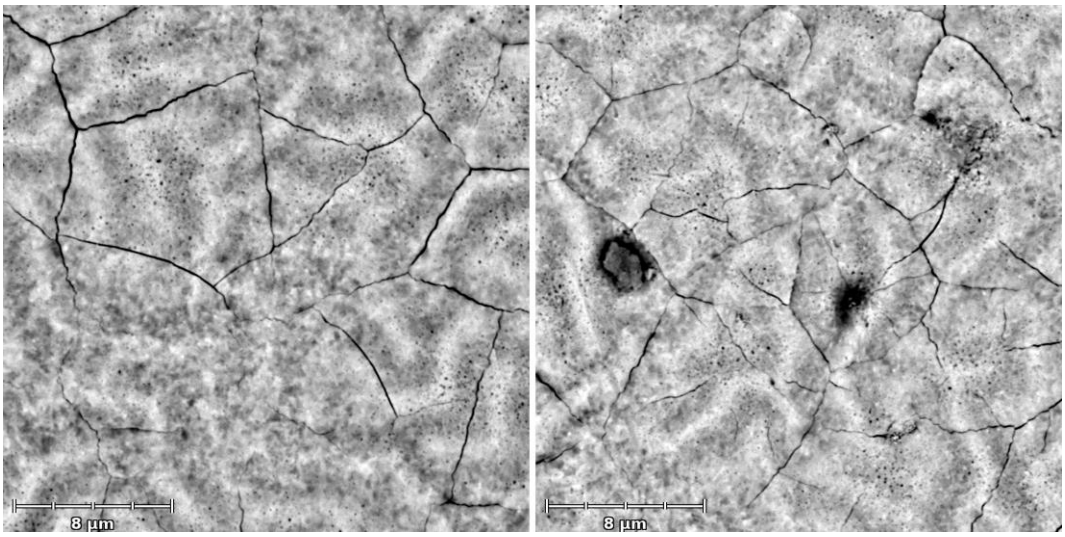

Figure 4.11: SEM images of the $MAPbI_3$ full stack dummy cell before and after 768 h of UV exposure.

To evaluate the UV shielding contribution of the glass substrate, CsFAMA complete dummy cells were characterised without the rigid glass support (Figure 4.12), exposing the full stack to the unfiltered 365 nm UV dose along the 768-hour experiment, representing a more realistic scenario for lightweight flexible PSCs intended for space applications. Despite the absence of the glass substrate, the optical response of the complete CsFAMA stack remained essentially unchanged throughout the experiment. The absorbance spectra recorded after 69 h and 768 h almost completely overlap the initial spectrum, demonstrating that direct UV exposure does not induce measurable photochemical degradation of the device stack. These results indicate that the excellent UV stability previously observed for CsFAMA cannot be attributed solely to the progressive UV filtering effect of the soda-lime glass substrate. Instead, the photostability appears to be an intrinsic property of the mixed-cation perovskite composition and its associated device architecture. This observation is particularly relevant for space applications, where flexible photovoltaic systems are expected to operate without heavy protective glass covers in order to maximise their specific power.

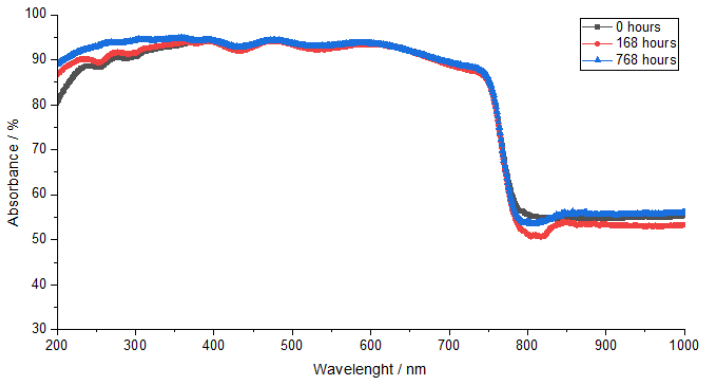

Figure 4.12: UV-VIS absorbance spectra of the non-supported CsFAMA full stack after various levels of UV exposure.

SEM analysis of the glass-free sample after UV exposure is presented in Figure 4.13. After-exposure SEM image presents prominent parallel ridge-like features and apparent delamination zones that are entirely absent in the before-exposure image. This contrasts with the UV-VIS data obtained for these same samples, which show no clear sign of degradation over the 768 hour exposure time. As such, the more plausible explanation is that these defects result from the mechanical handling of the unsupported flexible substrate during sample preparation and SEM characterisation. Without the soda-lime glass support, the PEN based substrate is more susceptible to bending, which could cause the cracking and delamination patterns observed in the SEM image. To conclusively distinguish mechanical damage from genuine UV-induced morphological degradation, additional control samples subjected to identical handling conditions but without UV exposure would be required. Nonetheless, the consistency of the UV-VIS optical data across all three time points remains a reliable indicator of the photochemical stability of the CsFAMA perovskite composition under unfiltered UV exposure.

Concluding, these results demonstrate that the remarkable UV stability of the CsFAMA devices is primarily governed by the intrinsic stability of the mixed-cation perovskite rather than by the shielding effect of the supporting glass substrate. This finding further supports the suitability of flexible inverted CsFAMA PSCs for lightweight space photovoltaic applications, where the elimination of protective glass can substantially reduce system mass without compromising photostability.

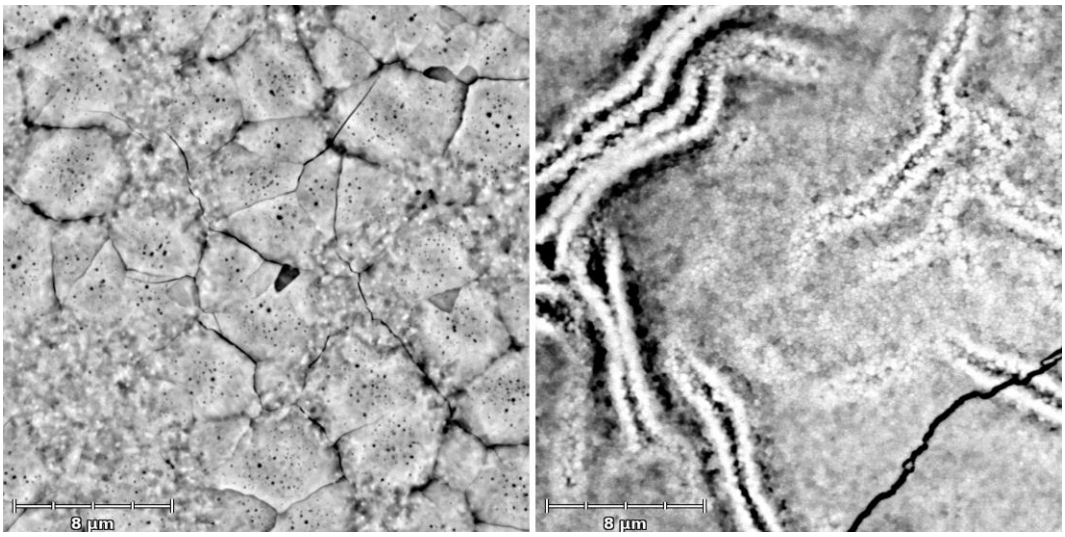

Figure 4.13: SEM images of the non-supported CsFAMA full stack dummy cell before and after 768 h of UV exposure.

In summary, the UV-VIS spectrophotometry study reveals a clear hierarchy of UV sensitivity across the PSC constituent layers. The organic components of the stacks like the PEN substrate and PTAA hole transport layer are the most UV-sensitive, exhibiting progressive optical changes even in an inert atmosphere and in the presence of the filtering effect from the glass substrate. The glass substrate itself undergoes slow solarisation, modifying the effective UV dose reaching the inner layers over time. In contrast, the CsFAMA perovskite absorber demonstrates exceptional photostability, maintaining its optical properties intact over 768 hours of UV irradiation, even without the glass UV filter. The $MAPbI_3$ absorber, by contrast, undergoes irreversible photodecomposition to PbI_2 evidenced both by the UV-VIS absorbance changes, the macroscopic yellowing of the irradiated area, and SEM morphological degradation. This confirms that compositional engineering via mixed-cation formulations is a critical requirement for UV-stable perovskite absorbers in space photovoltaic applications.

4.2.2. UV degradation on complete devices

Complementing the optical characterisation presented in Section 4.2.1, the photovoltaic performance of the fabricated PSCs was monitored during UV exposure over seven measurement intervals spanning 0 to 583 hours. Current density–voltage (*J*–*V*) measurements were performed under AM1.5 illumination at each interval, and the corresponding AM0 performance was estimated using the Python model described in Appendix A1. The extracted photovoltaic parameters were normalised to the value of each measured on the day of fabrication, allowing the retained device performance to be directly compared throughout the experiment. Control devices were stored in the dark under nitrogen atmosphere inside the glovebox and characterised at the same intervals, providing a baseline against which UV-induced degradation could be distinguished from natural ageing. The

$MAPbI_3$ and CsFAMA absorbers were studied separately. For the CsFAMA composition, an additional group of non-supported devices without the soda-lime glass support was included to assess the impact of the glass substrates as UV filters.

To mechanistically deconvolute the degradation pathways responsible for the observed photovoltaic losses, electrochemical impedance spectroscopy (EIS) was performed after 583 h UV exposure. EIS provides complementary information on the electrical processes occurring within the device by probing its frequency- dependent impedance response. Changes in the Nyquist spectra can therefore be directly correlated with the structural and optical degradation observed by UV–VIS spectroscopy and the loss of photovoltaic performance measured from the J–V characteristics [30].

The $MAPbI_3$ control devices exhibited stable photovoltaic performance throughout the experiment, as shown in Figure 4.14. Although some device-to-device variability is evident and characteristic of $MAPbI_3$ -based PSCs [31], particularly in the normalised PCE, no systematic deterioration of any photovoltaic parameter was observed over the 583 h monitoring period. The slight increase in V_{OC} observed during the first measurement intervals is characteristic of the burn-in effect commonly reported for $MAPbI_3$ PSCs and is generally attributed to photoinduced defect passivation together with ionic redistribution under the built-in electric field [31-32]. The absence of significant performance losses confirms that storage under nitrogen and the repeated characterisation protocol did not induce measurable degradation over the investigated timescale. Consequently, any additional degradation observed in the UV-exposed devices can be primarily attributed to UV irradiation.

In contrast, the $MAPbI_3$ devices subjected to UV irradiation exhibited rapid and irreversible degradation of all photovoltaic parameters (Figure 4.15). Performance losses were already evident after only 22 h of irradiation and became substantially more pronounced within the first 44 h, indicating that UV-induced degradation is initiated shortly after exposure. Although a slight recovery is observed around 65 h, this behaviour is consistent with the transient burn-in effect also present in the control devices and does not alter the overall degradation trend. After prolonged exposure, J_{SC} and PCE exhibited the largest losses, with their retained fractions approaching zero by the end of the experiment, while V_{OC} and FF also decreased progressively [31-32]. The rapid loss of J_{SC} is fully consistent with the optical characterisation presented in Section 4.2.1, where UV–VIS spectroscopy revealed the progressive bleaching of the characteristic $MAPbI_3$ absorption edge together with the appearance of the PbI_2 absorption features. These observations indicate that UV irradiation promotes the photodecomposition of the perovskite absorber, reducing the amount of photoactive material available for light harvesting and consequently suppressing

photocurrent generation [20]. The simultaneous decrease in V_{OC} is consistent with the formation of additional non-radiative recombination centres arising from both perovskite decomposition and UV-induced degradation of the PTAA hole-transport layer [28]. Likewise, the reduction in FF suggests increasing transport losses associated with deteriorated interfaces and less efficient charge extraction. The clear contrast with the control devices demonstrates that these performance losses originate predominantly from UV-induced degradation rather than from natural ageing.

The impedance measurements provide independent electrical confirmation of these degradation processes. As shown in the control plot in Figure 4.16, the Nyquist spectrum of the $MAPbI_3$ control device exhibits a single well-defined semicircular arc, characteristic of a healthy inverted PSC dominated by a single recombination process at the perovskite/transport-layer interfaces. The relatively small series resistance and the absence of additional low-frequency features indicate that the electrical properties of the device remained largely unchanged after prolonged storage under nitrogen, in agreement with the stable photovoltaic performance observed in Figure 4.14.

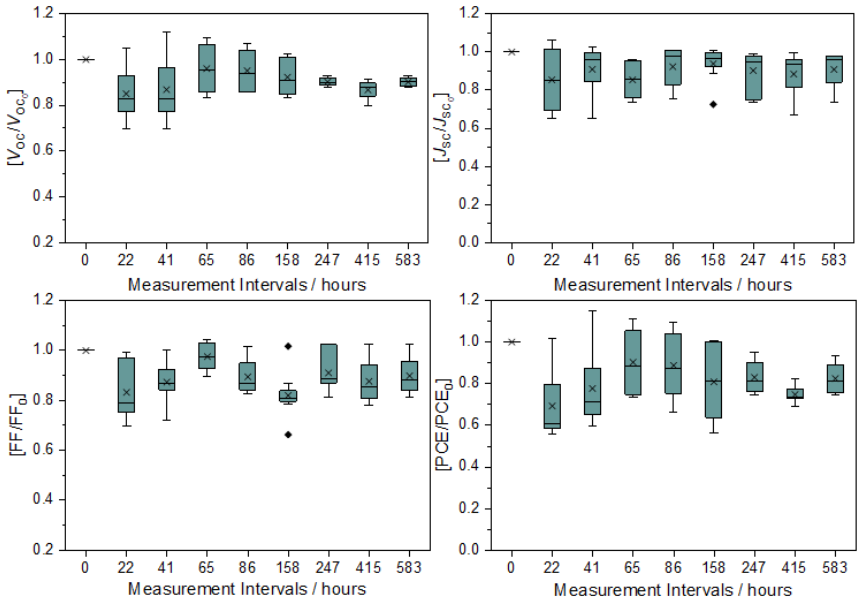

Figure 4.14: Evolution of the normalised photovoltaic parameters of the $MAPbI_3$ control devices over 583 h of storage under nitrogen atmosphere in the dark. All parameters were normalised to the value measured on the day of fabrication.

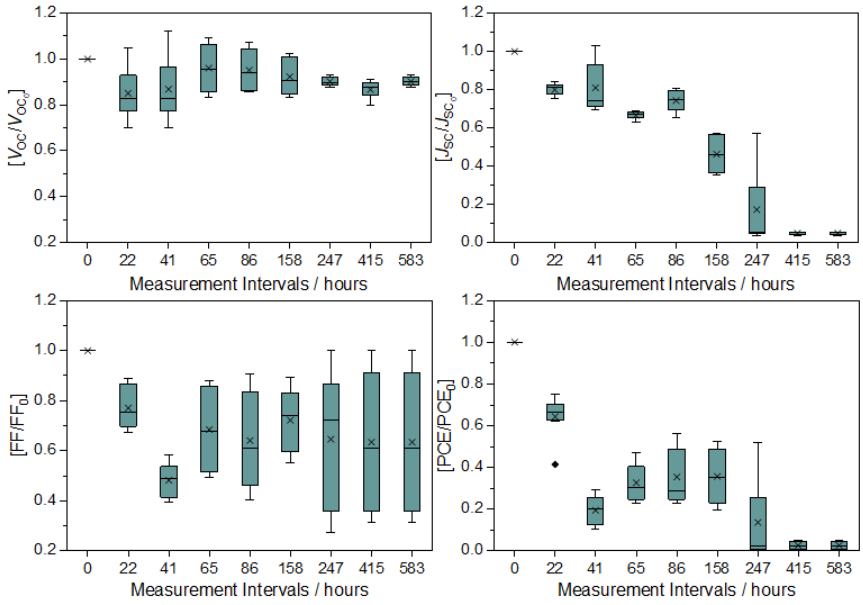

Figure 4.15: Evolution of the normalised photovoltaic parameters of the UV-exposed $MAPbI_3$ devices over 583 h of storage under nitrogen atmosphere. All parameters were normalised to the value measured on the day of fabrication.

In contrast, the Nyquist spectrum of the UV-exposed $MAPbI_3$ device (Figure 4.16) differs markedly from that of the control. Instead of a well-defined semicircular arc, the impedance response becomes nearly linear and extends to resistance values exceeding 3 MΩ, more than two orders of magnitude higher than those of the control device. Such behaviour is characteristic of a severely degraded photovoltaic device in which efficient charge transport has been almost completely suppressed. This electrical response is consistent with the extensive conversion of the photoactive $MAPbI_3$ absorber into electrically insulating PbI_2, as previously suggested by the UV–VIS spectra and corroborated by the severe collapse of J_{SC} and PCE. Therefore, the EIS measurements independently validate the conclusions drawn from the optical and photovoltaic characterisation, confirming that prolonged UV exposure leads to catastrophic and irreversible degradation of $MAPbI_3$ PSCs.

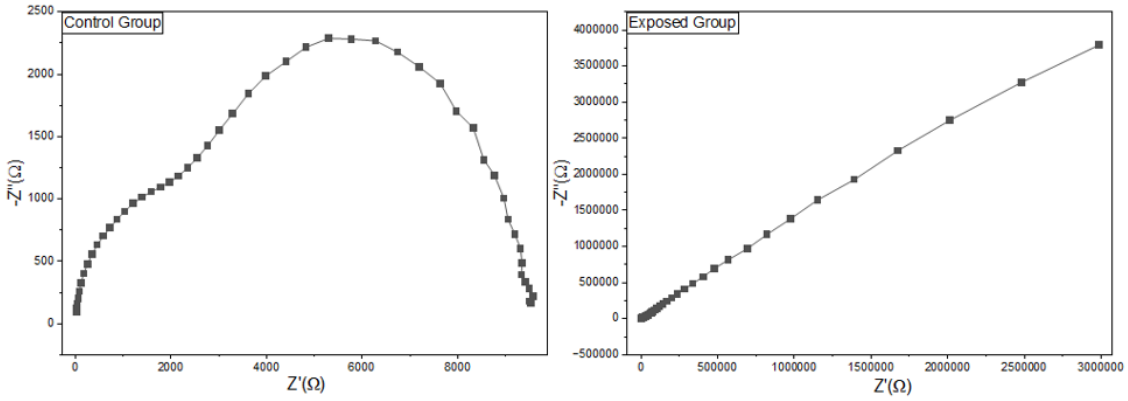

Figure 4.16: Nyquist Plots of the $MAPbI_3$ device after 583 h of storage under nitrogen atmosphere in the dark (left) and under UV exposure (right).

The CsFAMA control devices exhibited stable photovoltaic performance throughout the experiment, as shown in Figure 4.17. All four normalised photovoltaic parameters remained within a relatively narrow and stable range throughout the 583-hour measurement period, with only a slight downward trend observed at the latest measurement intervals. Although a few isolated outliers appeared towards the end of the experiment, particularly for PCE and FF, the overall distributions remained stable, and no systematic degradation was detected. These isolated deviations are most likely associated with device-to-device variability or contact-related artefacts rather than intrinsic degradation of the devices. Consequently, the control group provides a reliable baseline for distinguishing UV-induced degradation from natural ageing.

In contrast to the catastrophic degradation observed for $MAPbI_3$, the CsFAMA devices exposed to UV irradiation retained most of their photovoltaic performance throughout the experiment (Figure 4.18). Although all photovoltaic parameters exhibited a gradual decline with increasing exposure time, the degradation remained comparatively moderate, and the devices preserved meaningful photovoltaic activity even after 583 h of continuous UV irradiation. Among the four parameters, V_{OC} and J_{SC} proved to be the most stable, exhibiting only modest reductions throughout the ageing period. In contrast, PCE and the FF displayed a gradual and nearly monotonic decrease, suggesting that the dominant degradation mechanism primarily affects charge transport and extraction rather than photon absorption or photocarrier generation. This behaviour is fully consistent with the optical characterisation presented in Section 4.2.1. Unlike $MAPbI_3$, whose UV–VIS spectra showed progressive bleaching of the absorption edge and the formation of PbI_2, the CsFAMA absorber exhibited virtually no measurable optical changes after prolonged UV exposure. The preservation of the optical absorption together with the relatively stable J_{SC} indicates that the mixed-cation mixed-halide perovskite absorber remains chemically and optically intact throughout the experiment. Therefore, the gradual reduction in FF and PCE is unlikely to originate from degradation of the absorber itself and instead suggests progressive deterioration of the charge-transport interfaces. This interpretation is consistent with previous reports describing UV-induced photodegradation of the PTAA hole-transport layer [28]. The formation of interfacial trap states increases non-radiative recombination and reduces charge extraction efficiency without significantly affecting the optical absorption of the perovskite layer. Consequently, the superior UV stability of the CsFAMA devices can be primarily attributed to the improved intrinsic photostability of the mixed-cation perovskite composition, while the remaining performance losses appear to originate predominantly from interfacial degradation rather than bulk decomposition of the absorber [23].

The impedance measurements provide further evidence supporting an interface and transport-related degradation mechanism in the CsFAMA devices. As shown in Figure 4.19, the control device exhibits a comparatively small and well-defined impedance arc, consistent with the preserved photovoltaic performance observed throughout the ageing experiment. In contrast, after 583 h of UV exposure (Figure 4.19, on the right), the impedance magnitude increases by more than one order of magnitude and the Nyquist response becomes markedly broader and more complex, indicating substantial changes in the electrical processes governing charge transport and interfacial recombination within the device. Importantly, this pronounced electrical degradation occurs despite the absence of significant changes in the UV–VIS spectra, demonstrating that the dominant degradation mechanism is interfacial rather than bulk. The modified Nyquist response, including the appearance of overlapping impedance contributions, further suggests that more than one interfacial or transport process contributes to the degradation [28].

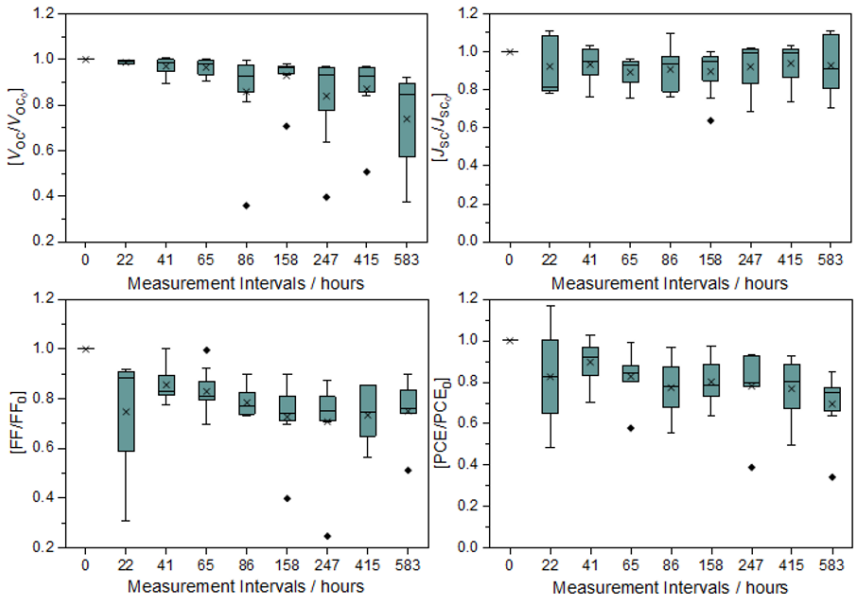

Figure 4.17: Evolution of the normalised photovoltaic parameters of the supported CsFAMA control devices over 583 h of storage under nitrogen atmosphere in the dark. All parameters were normalised to the value measured on the day of fabrication.

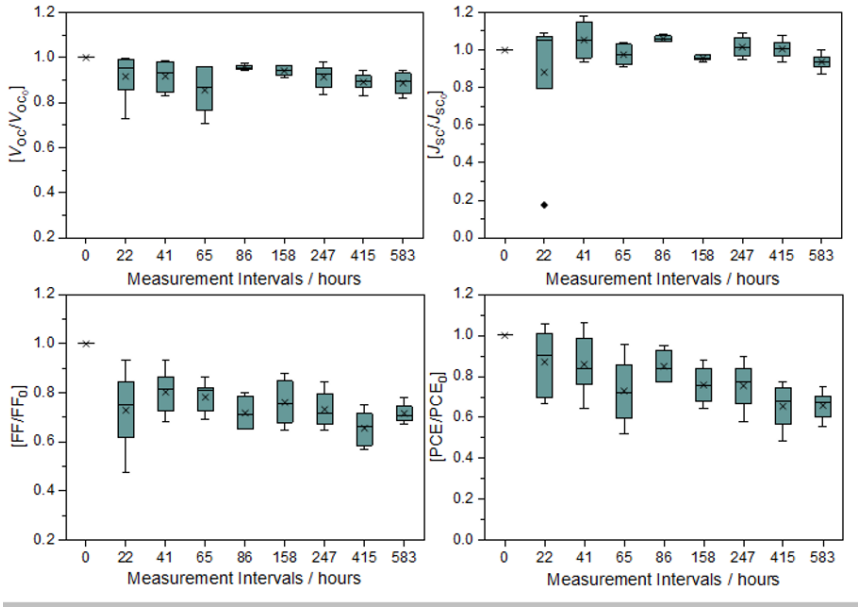

Figure 4.18: Evolution of the normalised photovoltaic parameters of the UV-exposed supported CsFAMA devices over 583 h of storage under nitrogen atmosphere. All parameters were normalised to the value measured on the day of fabrication.

Overall, the EIS measurements independently corroborate the conclusions obtained from both the optical and photovoltaic characterisation. Together, the UV–VIS, *J–V* and impedance results consistently demonstrate that prolonged UV exposure primarily degrades the charge-transport interfaces while leaving the CsFAMA absorber largely intact. This behaviour contrasts sharply with that of $MAPbI_3$, where all three characterisation techniques indicate extensive degradation of the photoactive absorber, highlighting the substantially improved UV resilience of the mixed-cation CsFAMA composition.

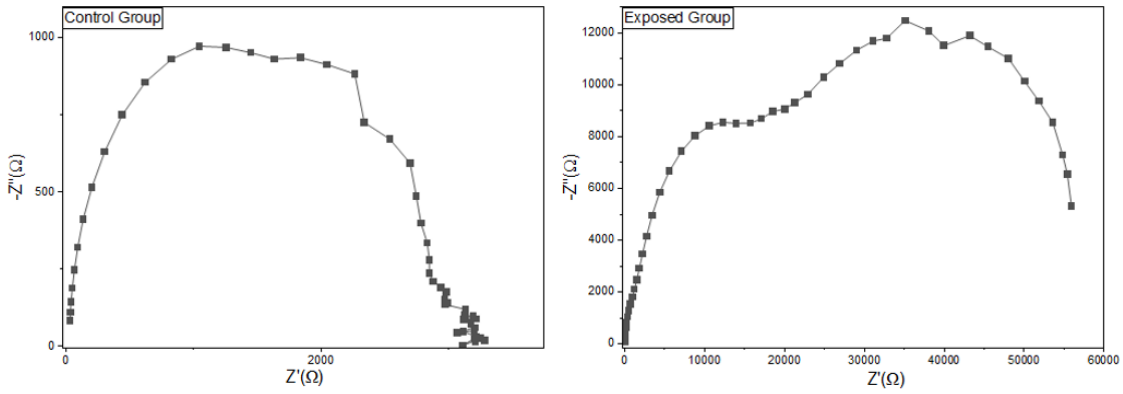

Figure 4.19: Nyquist Plots of the supported CsFAMA device after 583 h of storage under nitrogen atmosphere in the dark (left) and under UV exposure (right).

The non-supported CsFAMA control device exhibited a different baseline behaviour from its glass-supported counterpart (Figure 4.20). Most notably, the initial V_{OC} values were

consistently lower throughout the experiment, indicating that the removal of the temporary soda-lime glass support adversely affected the initial device performance. Although the exact origin of this behaviour cannot be established unequivocally, it is most likely associated with the mechanical stresses introduced during the detachment of the flexible substrate from the supporting glass and the subsequent handling of the device. Such mechanical stresses are known to induce microcracking of the ITO electrode and local interfacial delamination, both of which can reduce the electrical performance of flexible PSCs. Despite the lower initial performance, the photovoltaic parameters remained relatively stable over the 583 h monitoring period. Only a slight decrease in FF and PCE was observed, consistent with gradual mechanical deterioration rather than progressive degradation of the perovskite absorber. It should be noted that only a single device was available for this study, preventing a statistical analysis comparable to that performed for the supported devices.

Interestingly, the UV-exposed non-supported device (Figure 4.21) exhibited essentially the same degradation trend as its corresponding control. Although its initial photovoltaic performance was lower than that of the glass-supported devices, no additional systematic deterioration attributable exclusively to UV irradiation was observed. Instead, both the control and irradiated devices displayed comparable reductions in FF and PCE throughout the experiment. These observations are fully consistent with the optical characterisation presented in Section 4.2.1, which demonstrated that the CsFAMA absorber undergoes negligible optical degradation under prolonged UV exposure. Consequently, the performance losses observed in the unsupported flexible devices are more plausibly attributed to mechanically induced defects generated during substrate removal and handling than to direct UV-induced degradation of the perovskite absorber. Therefore, under the conditions investigated, the absence of the soda-lime glass support and consequently of its UV-filtering effect does not appear to significantly accelerate degradation of the CsFAMA perovskite itself.

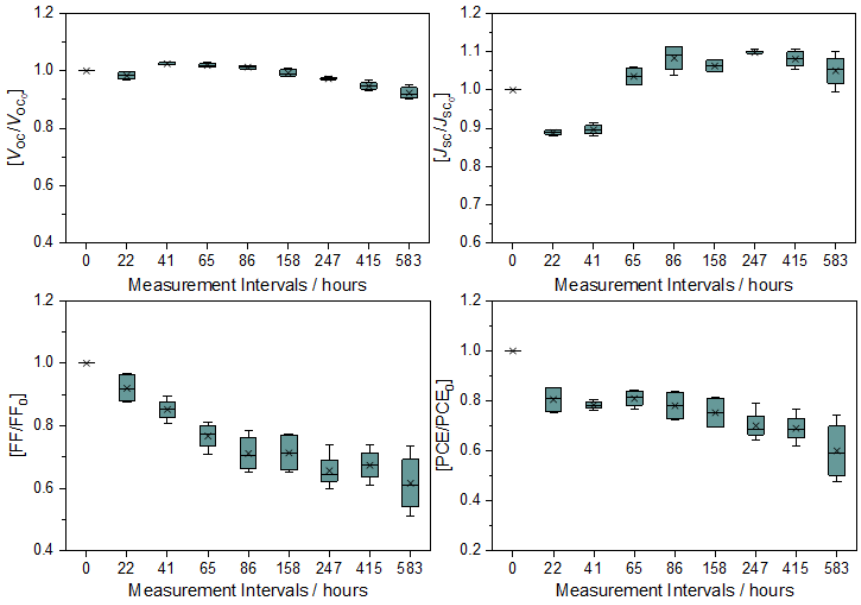

Figure 4.20: Evolution of the normalised photovoltaic parameters of the non-supported CsFAMA control devices over 583 h of storage under nitrogen atmosphere in the dark. All parameters were normalised to the value measured on the day of fabrication.

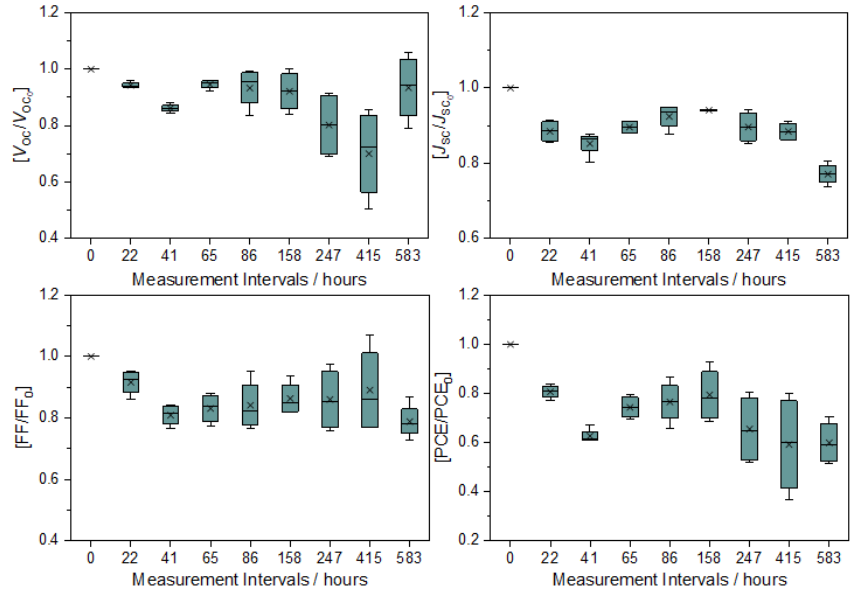

Figure 4.21: Evolution of the normalised photovoltaic parameters of the UV-exposed non-supported CsFAMA devices over 583 h of storage under nitrogen atmosphere. All parameters were normalised to the value measured on the day of fabrication.

The impedance measurements further support this interpretation. As shown in the control plot in Figure 4.22, the Nyquist spectrum of the flexible CsFAMA control device exhibits a complete semicircular arc characteristic of a functional photovoltaic device. However, the arc diameter is approximately 4.6 times smaller than that of the supported CsFAMA control device, indicating a substantially lower recombination resistance even before UV exposure. This elevated baseline recombination is consistent with the presence of mechanically

induced defects, such as ITO microcracks or partial interfacial delamination, which increase carrier recombination and reduce charge collection efficiency.

Following prolonged UV exposure (Figure 4.22), the impedance response changes dramatically. Unlike the supported CsFAMA device, which retains a well-defined semicircular arc despite a reduction in recombination resistance, the flexible UV-exposed device exhibits a large open arc extending into the hundreds of kΩ without returning to the real axis within the accessible frequency range. The persistent curvature of the spectrum indicates that the device retains a capacitive response characteristic of an intact perovskite absorber, distinguishing it from the nearly linear response observed for the severely degraded $MAPbI_3$ devices. However, the exceptionally high impedance demonstrates that efficient charge transport has become severely restricted.

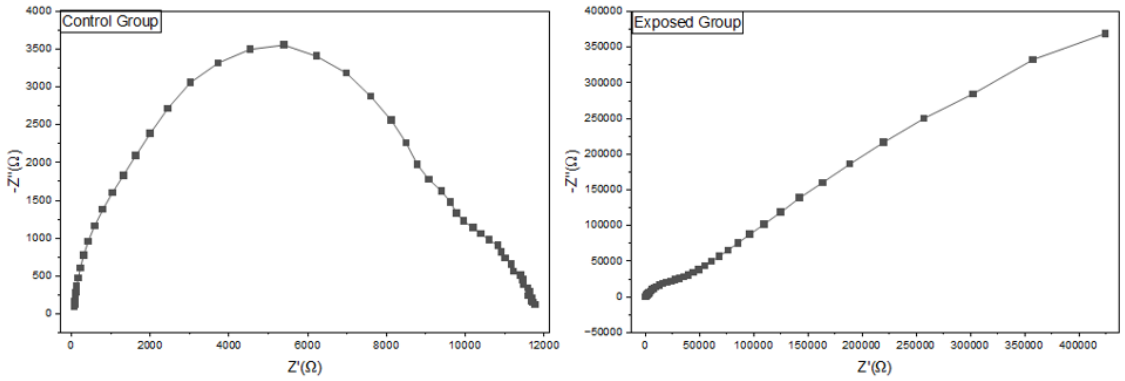

Figure 4.22: Nyquist Plots of the non-supported CsFAMA device after 583 h of storage under nitrogen atmosphere in the dark (left) and under UV exposure (right).

This behaviour is consistent with the simultaneous contribution of two degradation mechanisms. The first is the UV-induced deterioration of the PTAA hole-transport layer, which increases interfacial recombination and reduces hole extraction efficiency. The second is the restriction of lateral charge collection caused by mechanically induced microcracks in the ITO electrode. The combined action of these mechanisms provides a plausible explanation for the substantially larger impedance response observed in the unsupported flexible device compared with the supported CsFAMA device.

Overall, the results obtained from the *J–V* measurements and impedance spectroscopy indicate that the degradation of the non-supported CsFAMA devices is dominated by mechanically induced electrical defects rather than by photochemical degradation of the perovskite absorber. This finding reinforces the conclusions drawn from the UV–VIS characterisation, demonstrating that the mixed-cation CsFAMA composition possesses excellent intrinsic resistance to prolonged UV irradiation. Consequently, for flexible perovskite solar cells intended for space applications, improving the mechanical robustness

of the transparent conductive electrode and the transport-layer interfaces may become more critical than further enhancing the UV stability of the perovskite absorber itself.

4.3. Effects of High-Vacuum Degradation on the PSCs Performance

For the study of the influence of high-vacuum exposure on the photovoltaic performance of complete inverted PSCs, devices were exposed to a constant pressure of 7.5×10^{-7} mbar for cumulative exposure durations of 3, 6, and 8 hours. This pressure regime falls within the range characteristic of Low Earth Orbit (LEO), where ambient pressures typically span 10^{-4} to 10^{-6} Pa [8]. Between measurements, all samples were stored in dark conditions in the glovebox to eliminate degradation associated with oxygen, moisture or illumination. Photovoltaic characterisation was performed immediately before and after each vacuum exposure under simulated AM1.5 illumination, and the resulting *J-V* characteristics were converted to their AM0 equivalents using the methodology described in Section 3.5. Similarly to the methodology in previous sections, all photovoltaic parameters were normalised to the value measured on the fabrication day. Control devices stored under identical conditions but without vacuum exposure were characterised in parallel to distinguish vacuum-induced degradation from natural ageing and burn-in stabilisation.

Two absorber compositions were investigated, $MAPbI_3$ and CsFAMA, both employing the flexible inverted p–i–n architecture described previously.

Important to highlight that all PSCs had already experienced high-vacuum conditions during fabrication, as the silver back electrode was deposited by thermal evaporation. Bhowmik *et al*. [32] demonstrated that the thermal radiation emitted by the evaporation source promotes preferential iodide loss from the near-surface region of the perovskite, creating an iodide-deficient, trap-rich layer. Under these conditions, $MAPbI_3$ films exhibited an approximately 70% reduction in carrier lifetime, whereas an MA-free mixed-cation composition showed a significantly smaller reduction of around 30%, highlighting the greater resilience of compositionally engineered perovskites.

Interestingly, the same study also showed that radiation-free high-vacuum exposure has the opposite effect. Following 120 min of vacuum exposure without thermal radiation, carrier lifetimes increased to 8.08 ns, an improvement attributed to the removal of volatile residual impurities and surface adsorbates from the perovskite surface [32]. Consequently, the perovskite/PCBM interfaces of the devices investigated in this work cannot be considered pristine, as they already contain a certain degree of surface disorder introduced during Ag deposition. At the same time, the vacuum conditions employed in the present study may partially counteract these defects through interface cleaning. Therefore, the overall device response should be interpreted as the result of two competing mechanisms: pre-existing

fabrication-induced damage and the potentially beneficial effects of radiation-free high-vacuum exposure.

Figure 4.23 presents the normalised photovoltaic parameters (V_{oc}/V_{oc0}, J_{sc}/J_{sc0}, FF/FF$_0$ and PCE/PCE$_0$) of the $MAPbI_3$ devices after 3, 6 and 8 h, comparing the control group with devices exposed to dark high-vacuum conditions (7.5×10^{-7} mbar). Across all three intervals, the control devices display a pronounced and consistent improvement relative to their initial performance, with V_{oc}/V_{oc0} increasing to approximately 1.6–1.7 and PCE/PCE$_0$ to approximately 1.5–1.6, accompanied by a similar rise in FF/FF$_0$ (1.3–1.4). In contrast, J_{sc}/J_{sc0} shows only a slight decrease (0.86 – 0.93). This behaviour is consistent with burn-in stabilisation during the measurement period.

The vacuum-exposed devices do not display the same stabilisation effect. V_{OC}/V_{OC0} increases only modestly, remaining close to 1.05–1.1 at all three exposure times, while FF/FF$_0$ and PCE/PCE$_0$ both decrease consistently relative to their initial values, settling at approximately 0.78–0.83 and 0.83–0.93 respectively across the 3, 6 and 8 h intervals. J_{sc}/J_{sc0} also decreases slightly, although the larger spread observed after 8 h indicates increased device-to-device variability. Overall, these results suggest that dark high-vacuum exposure suppresses the burn-in-related gains observed in the control devices and introduces a moderate but consistent performance penalty, mainly reflected in FF and PCE.

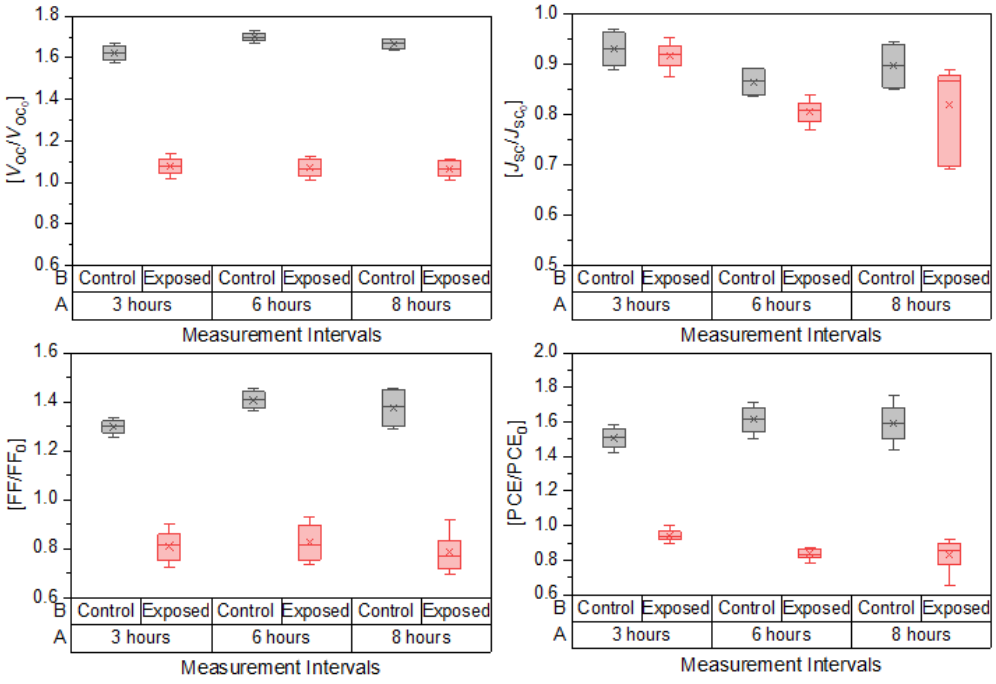

Figure 4.23: Photovoltaic Parameters for $MAPbI_3$ after vacuum exposure (Control vs Exposed).

The normalised photovoltaic parameters of the CsFAMA devices are presented in Figure 4.24, comparing the control group with devices exposed to dark high-vacuum conditions

(7.5×10^7 mbar) after 3, 6 and 8 h. The control devices exhibit a pronounced increase in V_{oc}/V_{oc0} (2.6 up to 3.8) and PCE/PCE$_0$ (2.1 up to 4.2) with increasing measurement time, while J_{sc}/J_{sc0} remains comparatively stable (0.72–0.80). This behaviour is consistent with a prolonged stabilisation process in the CsFAMA devices, potentially associated with ionic redistribution and defect passivation [31]. The comparatively low initial performance of this device batch may also amplify the normalised improvement ratios. Importantly, no systematic performance loss is observed in the control group, confirming that storage under inert atmosphere does not induce measurable degradation and providing a suitable reference for evaluating the effect of vacuum exposure.

The vacuum-exposed CsFAMA devices, in contrast, do not share this trajectory. The most evident difference is observed in V_{oc}, which remains substantially below the control values at all measurement intervals. Consequently, PCE also remains considerably lower than that of the control devices and shows no evidence of the progressive improvement observed under inert storage. These results indicate that high-vacuum exposure interferes with the electrical stabilisation process responsible for the performance gains of the control devices.

The evolution of J_{sc} and FF is less conclusive. Although their median values tend to decrease with increasing vacuum exposure time, the exposed devices exhibit substantial device-to-device variability, particularly after 6 and 8 h. The broad and overlapping distributions prevent a clear distinction between a systematic time-dependent degradation process and the intrinsic variability of the investigated devices. Therefore, the present dataset does not provide sufficient evidence to conclude that high-vacuum exposure causes progressive degradation of J_{sc} or FF over the investigated timescale. Indeed, the results demonstrate that dark high-vacuum exposure modifies the short-term evolution of CsFAMA PSC performance, primarily by suppressing the pronounced stabilisation observed in the control devices. A direct vacuum-induced degradation mechanism cannot, however, be established from the present dataset due to the limited number of devices, the large inter-device variability and the short exposure times. The absence of the vacuum-induced performance improvement reported by Bhowmik *et al.* [32] further suggests that the response of PSCs to vacuum exposure may depend strongly on device architecture, composition and experimental conditions. Longer exposure times and larger device populations are therefore required to determine the long-term stability of CsFAMA PSCs under high-vacuum conditions.

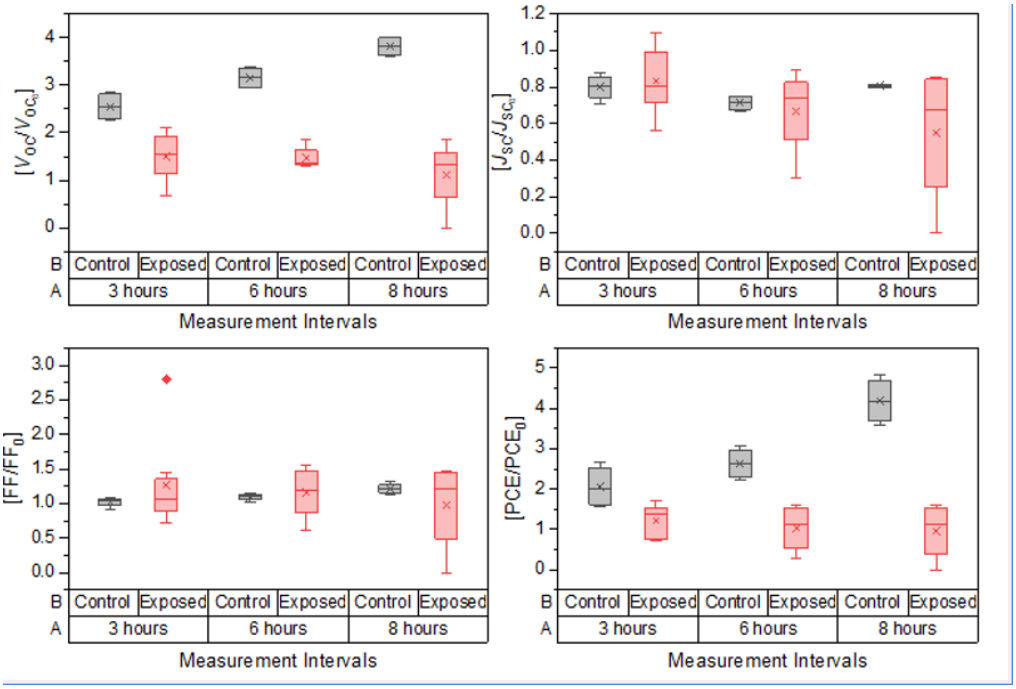

Figure 4.24: Photovoltaic Parameters for CsFAMA after vacuum exposure (Control vs Exposed).

5. Conclusions

This work investigated the predicted photovoltaic performance of flexible inverted p-i-n PSCs under the extraterrestrial AM0 spectrum and their degradation under prolonged UV irradiation and high-vacuum exposure (7.5×10^{-5} Pa). Two perovskite absorber compositions, $MAPbI_3$ and $Cs_{0.05}(FA_{0.85}MA_{0.15})_{0.95}Pb(I_{0.85}Br_{0.15})_3$ (referred to as CsFAMA for brevity), were investigated using flexible PEN-ITO substrates either mechanically supported on glass or tested without the temporary glass support. The experimental study combined UV-VIS spectrophotometry of individual PSC layers using incomplete "dummy cells", *J-V* characterisation of complete devices over time, EIS after prolonged UV exposure, and SEM imaging before and after the UV exposure period. AM0 device performance was estimated from experimental AM1.5 *J–V* and EQE measurements using the numerical methodology developed in this work.

The UV-VIS study revealed distinct differences in the level of photosensitivity among the stack components. Both the temporary glass support and the flexible PEN-ITO substrate underwent optical changes during the 768 h UV exposure period, indicating that the UV dose reaching the underlying layers may evolve over time. The PTAA HTL layer also exhibited evidence of UV-induced degradation. More pronounced degradation was observed for the $MAPbI_3$ absorber, for which spectroscopy, SEM imaging and visual inspection consistently indicated irreversible photodecomposition and PbI_2 formation. On the other hand, the CsFAMA absorber retains its optical properties entirely intact, even when irradiated without the temporary glass support and therefore without its UV-filtering effect, demonstrating substantially greater intrinsic photostability than $MAPbI_3$ under the investigated conditions. These results identify CsFAMA as the more promising absorber composition for flexible PSCs.

These findings were also confirmed at the device level using the *J-V* characterization of complete PSC devices. $MAPbI_3$ PSCs suffered significant performance loss within hundreds of hours of UV exposure, with both J_{SC} and PCE approaching zero, suggesting that the composition is incompatible with space deployment in its current form. CsFAMA devices showed only moderate performance losses, retaining meaningful photoconversion efficiency at 583 h. Combined with the absence of measurable optical degradation of the CsFAMA absorber, these results indicate that the remaining performance losses are predominantly associated with degradation of the charge-transport layers and interfaces rather than decomposition of the perovskite absorber. EIS further supported this interpretation: the UV-exposed $MAPbI_3$ device exhibited an impedance increase of more than two orders of magnitude, consistent with the extensive absorber degradation identified by UV–VIS and SEM, whereas the CsFAMA devices retained a capacitive impedance response despite a pronounced

increase in impedance and substantial changes in the processes governing charge transport and interfacial recombination. Considering the UV sensitivity of PTAA, degradation of the hole-transport layer and the PTAA/perovskite interface provides a plausible explanation for this behaviour. Unsupported flexible CsFAMA devices exhibited an even more severe electrical response, consistent with the additional contribution of mechanically induced damage, possibly associated with ITO microcracking during substrate handling.

The high-vacuum study revealed a measurable, composition-dependent degradation response rather than a complete absence of vacuum effects. $MAPbI_3$ devices showed a modest but consistent penalty in FF and PCE relative to control across all exposure times, together with a marked suppression of the burn-in-related Voc and PCE gains seen in the control group. A similar suppression of the stabilisation process was observed for CsFAMA devices, particularly in V_{OC} and PCE. Although the median J_{SC} and FF values tended to decrease with increasing exposure time, the substantial device-to-device variability prevented the identification of a clear time-dependent degradation trend. These findings suggest that short-duration dark vacuum exposure at this level is not negligible and may constitute a measurable degradation pathway for inverted PSCs of these compositions, with CsFAMA appearing more susceptible than $MAPbI_3$ within the investigated window, though the limited sample sizes and exposure durations still limit definitive conclusions.

Overall, this work identifies CsFAMA as a substantially more promising absorber than $MAPbI_3$ for flexible PSCs intended for space applications due to its markedly superior intrinsic UV stability. The combined optical, photovoltaic and impedance results indicate that, once absorber photostability is improved, degradation of the charge-transport layers and interfaces becomes a dominant limitation, with the UV sensitivity of PTAA providing a plausible contribution to the observed performance losses. In addition, the poorer electrical response of unsupported flexible devices highlights mechanical integrity, possibly including ITO microcracking during handling, as an additional factor requiring optimisation. These findings demonstrate the need to address absorber stability, transport-layer and interface robustness, and the mechanical reliability of flexible devices together when developing and qualifying PSCs for operation in space-relevant environments.

6. Assessment of the work done

6.1. Objectives Achieved

The objectives defined were to estimate the photovoltaic performance of the fabricated PSCs under the extraterrestrial AM0 spectrum, investigate the effects of prolonged UV irradiation on the individual device components and complete PSCs, and evaluate the influence of high-vacuum exposure on device performance.

All objectives were completed. The AM0 performance estimation methodology enabled the photovoltaic behaviour of the fabricated devices under extraterrestrial illumination to be predicted from experimental AM1.5 *J–V* and *EQE* measurements, providing a practical approach for assessing device performance when dedicated AM0 solar simulation is unavailable. The UV exposure study successfully demonstrated the markedly higher photostability of CsFAMA compared with $MAPbI_3$ and identified charge-transport layers and interfaces, together with possible mechanically induced damage in unsupported flexible devices, as relevant degradation pathways. The high-vacuum study showed that vacuum exposure modifies the short-term electrical evolution of both compositions, although limited sample sizes and exposure times prevented definitive conclusions regarding vacuum-induced degradation and long-term stability.

6.2. Contribution to the Sustainable Development Goals

SDG	Target	Contribution	Performance Indicators and Metrics
SDG 7: Affordable and Clean Energy	7.2 - Substantially increase the share of renewable energy in the global energy mix	Investigates the stability of perovskite solar cells under UV radiation in simulated space conditions, directly contributing to the development of reliable solar energy sources for space applications.	-PCE retention (%) -Hours of stable operation under UV exposure -Ratio of functional to failed devices after exposure
	7.3 - Double the global rate of improvement in energy efficiency	Characterises fill factor (FF) degradation and recombination resistance (R_{rec}) changes, providing data to optimise efficiency and reduce energy losses in future space photovoltaic designs.	-FF retention (%) -R_{rec} values before and after UV exposure (kΩ)

SDG	Target	Contribution	Performance Indicators and Metrics
SDG 9: Industry, Innovation and Infrastructure	9.4 - Upgrade infrastructure and retrofit industries to make them sustainable and resource-efficient	Compares degradation of supported and non-supported flexible ITO substrates, identifying substrate-induced failure modes relevant to the development of lightweight, flexible space solar panels.	-J_{SC} and V_{OC} degradation rates (%) -Supported vs. non-supported performance comparison after UV exposure
	9.5 - Enhance scientific research and upgrade technological capabilities of industrial sectors	Advances fundamental understanding of perovskite degradation mechanisms through EIS characterisation, contributing to the scientific knowledge base for next-generation photovoltaics.	-Number of degradation mechanisms identified and characterised -EIS findings on ionic vs. electronic process contributions.
SDG 13: Climate Action	13.3 - Improve education and awareness on climate change mitigation, adaptation and impact reduction	Generates actionable data on absorber composition and substrate selection to extend the operational lifetime of space solar cells, directly informing design choices for low-carbon energy technologies.	-Estimated operational lifetime extension -Stability comparison between $MAPbI_3$ and CsFAMA absorbers under UV exposure.

6.3. Other Work Carried Out

No relevant additional work was carried out in the course of the current project.

6.4. Final Assessment

The objectives defined for this work were successfully addressed, providing relevant insights into the performance and stability of flexible PSCs under space-relevant conditions. The UV irradiation study yielded clear conclusions regarding the different degradation behaviour of $MAPbI_3$ and CsFAMA devices, while the high-vacuum study provided an initial assessment of their short-term response and identified the need for longer exposure times and larger device populations to establish definitive conclusions regarding vacuum-induced degradation and long-term stability.

7. References

[1] Space Foundation. (2024). *The Space Report 2024 Q2*. Space Foundation. https://www.spacefoundation.org/2024/07/18/the-space-report-2024-q2/

[2] National Renewable Energy Laboratory. (2026). *Best research-cell efficiencies* [Chart]. U.S. Department of Energy, Office of Energy Efficiency and Renewable Energy. https://www.nrel.gov/pv/assets/pdfs/best-research-cell-efficiencies.pdf

[3] Zhang, X., Han, D., Chen, X., Chen, Y., Chang, S., & Zhong, H. (2021). Effects of solvent coordination on perovskite crystallization. *Acta Physico-Chimica Sinica*, 37(4), Article 2008055. https://doi.org/10.3866/PKU.WHXB202008055

[4] Beygisangchin, M., Kamarudin, S. K., Umar, A. A., Farhadi, B., Baghdadi, A. H., Letchumanan, I., Rajabi, A., Ehsan, A. A., & Shaari, N. (2024). Advancements in configuration structures and fabrication techniques for achieving stability in perovskite solar cells: A comprehensive review. *Journal of the Korean Ceramic Society*, 61(5), 755–782. https://doi.org/10.1007/s43207-024-00401-0

[5] ASTM International. (2019). Standard solar constant and zero air mass solar spectral irradiance tables (ASTM E490-00a(2019)). https://www.astm.org/Standards/E490.htm

[6] ASTM International. (2020). Standard tables for reference solar spectral irradiances: Direct normal and hemispherical on 37° tilted surface (ASTM G173-03(2020)). https://www.astm.org/Standards/G173.htm

[7] Drabczyk, A., Uss, P., Bucka, K., Bulowski, W., Kasza, P., Putynkowski, G., & Socha, R. P. (2026). Space photovoltaics: Materials, device concepts and operational challenges. *Electronics*, *15*(10), Article 1978. https://doi.org/10.3390/electronics15101978

[8] Duarte, V. C. M., Santos, L. F., & Andrade, L. (2026). Perovskite solar cells for space applications: Progress, perspectives, and remaining challenges. *Energies*, *19*(6), Article 1432. https://doi.org/10.3390/en19061432

[9] Roy, P., Sinha, N. K., Tiwari, S., & Khare, A. (2020). A review on perovskite solar cells: Evolution of architecture, fabrication techniques, commercialization issues and status. *Solar Energy*, *198*, 665–688. https://doi.org/10.1016/j.solener.2020.01.080

[10] Kahandal, S. S., Tupke, R. S., Bobade, D. S., Kim, H., Piao, G., Sankapal, B. R., Said, Z., Pagar, B. P., Pawar, A. C., Kim, J. M., & Bulakhe, R. N. (2024). Perovskite solar cells: Fundamental aspects, stability challenges, and future prospects. *Progress in Solid State Chemistry*, *74*, Article 100463. https://doi.org/10.1016/j.progsolidstchem.2024.100463

[11] Gkinia, K. E., Antoniadou, M., Balis, N., Kaltzoglou, A., Kontos, A. G., & Falaras, P. (2019). Mixing cations and halide anions in perovskite solar cells. *Materials Today: Proceedings*, 19, 73–78. https://doi.org/10.1016/j.matpr.2019.07.344

[12] Jonathan, L., Diguna, L. J., Samy, O., Muqoyyanah, M., Abu Bakar, S., Birowosuto, M. D., & El Moutaouakil, A. (2022). Hybrid organic-inorganic perovskite halide materials for photovoltaics towards their commercialization. *Polymers*, 14(5), Article 1059. https://doi.org/10.3390/polym14051059

[13] Bashir, R. H., Inanc, I., Benahmedi, L., Moulebhar, S., Kuru, M., & Aissani, A. (2026). Fabrication and performance of $MAPbI_3$ perovskite solar cells under extreme humidity conditions: A spin-coating approach. *Solid State Sciences*, 174, Article 108227. https://doi.org/10.1016/j.solidstatesciences.2026.108227

[14] Chen, Z., Turedi, B., Alsalloum, A. Y., et al. (2019). Single-crystal $MAPbI_3$ perovskite solar cells exceeding 21% power conversion efficiency. *ACS Energy Letters*, *4*, 1258–1259. https://doi.org/10.1021/acsenergylett.9b00847

[15] Wang, S., Pang, S., Chen, D., Zhu, W., Xi, H., & Zhang, C. (2021). Improving perovskite solar cell performance by compositional engineering via triple-mixed cations. *Solar Energy*, 220, 412–417. https://doi.org/10.1016/j.solener.2021.03.036

[16] Saliba, M., Matsui, T., Seo, J. Y., Domanski, K., Correa-Baena, J. P., Nazeeruddin, M. K., Zakeeruddin, S. M., Tress, W., Abate, A., Hagfeldt, A., & Grätzel, M. (2016). Cesium-containing triple cation perovskite solar cells: Improved stability, reproducibility and high efficiency. *Energy & Environmental Science*, *9*(6), 1989-1997. https://doi.org/10.1039/C5EE03874J

[17] Yang, J., Bao, Q., Shen, L., & Ding, L. (2020). Potential applications for perovskite solar cells in space. *Nano Energy*,*76*, Article 105019. https://doi.org/10.1016/j.nanoen.2020.105019

[18] Rehan, M. S., Khan, A. D., Ahmad, N., & Ahmad, F. (2026). Towards sustainable and flexible solar energy: A review of perovskite solar cell technologies. *Energy Reports*, *15*, 109262. https://doi.org/10.1016/j.egyr.2026.109262

[19] Xu, R., Pan, F., Chen, J., Li, J., Yang, Y., Sun, Y., Zhu, X., Li, P., Cao, X., Xi, J., Xu, J., Yuan, F., Dai, J., Zuo, C., Ding, L., Dong, H., Jen, A. K.-Y., & Wu, Z. (2024). Optimizing the buried interface in flexible perovskite solar cells to achieve over 24% efficiency and long-term stability. *Advanced Materials*,*36*(34), Article 2308039 https://doi.org/10.1002/adma.202308039

[20] Jiang, Y., Yang, S. C., Jeangros, Q., Pisoni, S., Moser, T., Buecheler, S., Tiwari, A. N., & Fu, F. (2020). Mitigation of vacuum and illumination-induced degradation in perovskite solar cells by structure engineering. *Joule*, 4(5), 1087–1103. https://doi.org/10.1016/j.joule.2020.03.017

[21] Lee, S.-W., Kim, S., Bae, S., Cho, K., Chung, T., Mundt, L. E., Lee, S., Park, S., Park, H., Schubert, M. C., Glunz, S. W., Ko, Y., Jun, Y., Kang, Y., Lee, H.-S., & Kim, D. (2016).

UV degradation and recovery of perovskite solar cells. Scientific Reports, 6, 38150. https://doi.org/10.1038/srep38150

[22] Tayagaki, T., Kobayashi, H., Yamamoto, K., Murakami, T. N., & Yoshita, M. (2023). Ultraviolet-light-dark cycle analysis of degradation in perovskite solar cells. Solar Energy Materials and Solar Cells, 263, 112583. https://doi.org/10.1016/j.solmat.2023.112583

[23] Yang, J., Hong, Q., Yuan, Z., Xu, R., Guo, X., Xiong, S., Liu, X., Braun, S., Li, Y., Tang, J., Duan, C., Fahlman, M., & Bao, Q. (2018). Unraveling photostability of mixed cation perovskite films in extreme environment. Advanced Optical Materials, 6, 1800262. https://doi.org/10.1002/adom.201800262

[24] Haque, S., Alexandre, M., Vicente, A. T., Li, K., Schuster, C. S., Yang, S., Águas, H., Martins, R., Ferreira, R. A. S., & Mendes, M. J. (2024). Photon shifting and trapping in perovskite solar cells for improved efficiency and stability. Light: Science & Applications, 13, 238. https://doi.org/10.1038/s41377-024-01559-2

[25] Long, B. T., Peters, L. J., & Schreiber, H. D. (1998). Solarization of soda–lime–silicate glass containing manganese. Journal of Non-Crystalline Solids, 239(1–3), 126–130. https://doi.org/10.1016/S0022-3093(98)00728-5

[26] Scheirs, J., & Gardette, J.-L. (1997). Photo-oxidation and photolysis of poly(ethylene naphthalate). *Polymer Degradation and Stability*, *56*(3), 339–350. https://doi.org/10.1016/S0141-3910(96)00199-1

[27] Petrović, M., Maksudov, T., Panagiotopoulos, A., Serpetzoglou, E., Konidakis, I., Stylianakis, M. M., Stratakis, E., & Kymakis, E. (2019). Limitations of a polymer-based hole transporting layer for application in planar inverted perovskite solar cells. *Nanoscale Advances*, 1(8), 3107–3118. https://doi.org/10.1039/C9NA00246D

[28] Lin, C.-T., Pont, S., Kim, J., Du, T., Xu, S., Li, X., Bryant, D., McLachlan, M. A., & Durrant, J. R. (2018). Passivation against oxygen and light induced degradation by the PCBM electron transport layer in planar perovskite solar cells. *Sustainable Energy & Fuels*, 2(8), 1686–1692. https://doi.org/10.1039/C8SE00095F

[29] Zhang, Z., Wang, H., Jacobsson, T. J., & Luo, J. (2022). Big data driven perovskite solar cell stability analysis. *Nature Communications*, *13*, 7639. https://doi.org/10.1038/s41467-022-35400-4

[30] Klotz, D., Tumen-Ulzii, G., Qin, C., Matsushima, T., & Adachi, C. (2019). Detecting and identifying reversible changes in perovskite solar cells by electrochemical impedance spectroscopy. *RSC Advances*, 9, 33436–33445. https://doi.org/10.1039/c9ra07048f

[31] Khenkin, M. V., Katz, E. A., Abate, A., Bardizza, G., Berry, J. J., et al. (2020). Consensus statement for stability assessment and reporting for perovskite photovoltaics based on ISOS procedures. *Nature Energy*, *5*, 35–49. https://doi.org/10.1038/s41560-019-0529-5

[32] Bhowmik, K. K., Zhu, L., & Zhao, L. (2026). Degradation and self-healing of halide perovskites exposed to vacuum thermal evaporation environment. *Matter & Light*, 1, Article 100022. https://doi.org/10.1016/j.matlit.2026.100022

Appendix A – Characterization Methodology

A.1 Photovoltaic Characterization

Table A.1: Example of the Excel Sheet used in the photovoltaic characterization of the PSCs

Number	Time/s	Potential/V	Current/A	-(Potential/V)	Current /mA	J /mA·cm^{-2}	P /mW·cm^{-2}
1	0	-1.1	-1.13E-03	1.1	-1.13	-5.96	-6.55
2	0.5	-1.09	-1.08E-03	1.09	-1.08	-5.71	-6.25
3	1	-1.08	-9.88E-04	1.08	-0.988	-5.2	-5.64
4	1.5	-1.07	-8.95E-04	1.07	-0.895	-4.71	-5.06
5	2	-1.06	-8.04E-04	1.06	-0.804	-4.23	-4.51
6	2.5	-1.05	-7.15E-04	1.05	-0.715	-3.77	-3.97
7	3	-1.04	-6.28E-04	1.04	-0.628	-3.31	-3.46
8	3.5	-1.03	-5.39E-04	1.03	-0.539	-2.84	-2.93
9	4	-1.02	-4.50E-04	1.02	-0.45	-2.37	-2.43
10	4.5	-1.01	-3.61E-04	1.01	-0.361	-1.9	-1.93
11	5	-1	-2.69E-04	1	-0.269	-1.41	-1.42
12	5.5	-0.995	-1.75E-04	0.995	-0.175	-0.92	-0.915
13	6	-0.985	-7.77E-05	0.985	-0.0776	-0.409	-0.403
14	6.5	-0.98	-2.89E-05	0.98	-0.0289	-0.152	-0.149
15	7	-0.97	7.50E-05	0.97	0.075	0.395	0.383
16	7.5	-0.96	1.80E-04	0.96	0.18	0.95	0.912
17	8	-0.95	2.90E-04	0.95	0.29	1.53	1.45
18	8.8	-0.945	3.42E-04	0.945	0.342	1.8	1.7
19	9.3	-0.935	4.62E-04	0.935	0.462	2.43	2.27
20	9.8	-0.925	5.81E-04	0.925	0.581	3.06	2.83
21	10.3	-0.915	7.03E-04	0.915	0.703	3.7	3.39
22	10.8	-0.905	8.29E-04	0.905	0.829	4.36	3.95
23	11.3	-0.895	9.58E-04	0.895	0.958	5.04	4.51
24	11.8	-0.885	1.09E-03	0.885	1.09	5.73	5.07

25	12.3	-0.875	1.22E-03	0.875	1.22	6.43	5.63
26	12.8	-0.865	1.36E-03	0.865	1.36	7.15	6.18
27	13.3	-0.855	1.50E-03	0.855	1.5	7.87	6.73
28	13.8	-0.845	1.63E-03	0.845	1.63	8.59	7.26
29	14.3	-0.835	1.77E-03	0.835	1.77	9.32	7.78
30	14.8	-0.825	1.91E-03	0.825	1.91	10	8.29
31	15.3	-0.815	2.05E-03	0.815	2.05	10.8	8.77
32	15.8	-0.805	2.18E-03	0.805	2.18	11.5	9.24
33	16.3	-0.795	2.32E-03	0.795	2.32	12.2	9.69
34	16.8	-0.785	2.45E-03	0.785	2.45	12.9	10.1
35	17.3	-0.775	2.58E-03	0.775	2.58	13.6	10.5
36	17.8	-0.765	2.70E-03	0.765	2.7	14.2	10.9
37	18.3	-0.755	2.82E-03	0.755	2.82	14.9	11.2
38	18.8	-0.745	2.94E-03	0.745	2.94	15.5	11.5
39	19.3	-0.735	3.05E-03	0.735	3.05	16.1	11.8
40	19.8	-0.725	3.16E-03	0.725	3.16	16.6	12.1
41	20.3	-0.715	3.26E-03	0.715	3.26	17.2	12.3
42	20.8	-0.705	3.36E-03	0.705	3.36	17.7	12.5
43	21.3	-0.695	3.45E-03	0.695	3.45	18.1	12.6
44	21.8	-0.685	3.53E-03	0.685	3.53	18.6	12.7
45	22.3	-0.675	3.61E-03	0.675	3.61	19	12.8
46	22.8	-0.665	3.68E-03	0.665	3.68	19.4	12.9
47	23.3	-0.655	3.75E-03	0.655	3.75	19.7	12.9
48	23.8	-0.645	3.81E-03	0.645	3.81	20.1	12.9
49	24.3	-0.635	3.87E-03	0.635	3.87	20.4	12.9
50	24.8	-0.625	3.92E-03	0.625	3.92	20.6	12.9
51	25.3	-0.615	3.96E-03	0.615	3.96	20.9	12.8
52	26.1	-0.61	3.97E-03	0.61	3.97	20.9	12.8
53	26.6	-0.6	4.02E-03	0.6	4.02	21.1	12.7
54	27.1	-0.59	4.05E-03	0.59	4.05	21.3	12.6

55	27.6	-0.58	4.08E-03	0.58	4.08	21.5	12.5
56	28.1	-0.57	4.11E-03	0.57	4.11	21.6	12.3
57	28.6	-0.56	4.14E-03	0.56	4.14	21.8	12.2
58	29.1	-0.55	4.16E-03	0.55	4.16	21.9	12
59	29.6	-0.54	4.18E-03	0.54	4.18	22	11.9
60	30.1	-0.53	4.19E-03	0.53	4.19	22.1	11.7
61	30.6	-0.52	4.21E-03	0.52	4.21	22.2	11.5
62	31.1	-0.51	4.23E-03	0.51	4.23	22.2	11.3
63	31.6	-0.5	4.24E-03	0.5	4.24	22.3	11.1
64	32.1	-0.49	4.25E-03	0.49	4.25	22.4	11
65	32.6	-0.48	4.26E-03	0.48	4.26	22.4	10.8
66	33.1	-0.47	4.27E-03	0.47	4.27	22.5	10.6
67	33.6	-0.46	4.28E-03	0.46	4.28	22.5	10.4
68	34.1	-0.45	4.29E-03	0.45	4.29	22.6	10.1
69	34.6	-0.44	4.29E-03	0.44	4.29	22.6	9.94
70	35.1	-0.43	4.30E-03	0.43	4.3	22.6	9.72
71	35.6	-0.42	4.31E-03	0.42	4.31	22.7	9.51
72	36.1	-0.41	4.31E-03	0.41	4.31	22.7	9.3
73	36.6	-0.4	4.32E-03	0.4	4.32	22.7	9.08
74	37.1	-0.39	4.32E-03	0.39	4.32	22.7	8.86
75	37.6	-0.38	4.33E-03	0.38	4.33	22.8	8.65
76	38.1	-0.37	4.33E-03	0.37	4.33	22.8	8.43
77	38.6	-0.36	4.33E-03	0.36	4.33	22.8	8.2
78	39.1	-0.35	4.34E-03	0.35	4.34	22.8	7.99
79	39.6	-0.34	4.34E-03	0.34	4.34	22.8	7.76
80	40.1	-0.33	4.34E-03	0.33	4.34	22.9	7.54
81	40.6	-0.32	4.35E-03	0.32	4.35	22.9	7.31
82	41.1	-0.31	4.35E-03	0.31	4.35	22.9	7.09
83	41.6	-0.3	4.35E-03	0.3	4.35	22.9	6.87
84	42.1	-0.29	4.36E-03	0.29	4.36	22.9	6.64

85	42.6	-0.28	4.36E-03	0.28	4.36	22.9	6.42
86	43.1	-0.27	4.36E-03	0.27	4.36	23	6.19
87	43.6	-0.26	4.36E-03	0.26	4.36	23	5.96
88	44.1	-0.25	4.37E-03	0.25	4.37	23	5.74
89	44.6	-0.24	4.37E-03	0.24	4.37	23	5.51
90	45.1	-0.23	4.37E-03	0.23	4.37	23	5.29
91	45.6	-0.22	4.38E-03	0.22	4.38	23	5.06
92	46.1	-0.21	4.38E-03	0.21	4.38	23	4.83
93	46.6	-0.2	4.38E-03	0.2	4.38	23.1	4.6
94	47.1	-0.19	4.38E-03	0.19	4.38	23.1	4.37
95	47.6	-0.18	4.39E-03	0.18	4.39	23.1	4.15
96	48.1	-0.17	4.39E-03	0.17	4.39	23.1	3.92
97	48.6	-0.16	4.39E-03	0.16	4.39	23.1	3.69
98	49.1	-0.15	4.39E-03	0.15	4.39	23.1	3.46
99	49.6	-0.14	4.40E-03	0.14	4.4	23.1	3.23
100	50.1	-0.13	4.40E-03	0.13	4.4	23.1	3
101	50.6	-0.12	4.40E-03	0.12	4.4	23.2	2.77
102	51.1	-0.11	4.40E-03	0.11	4.4	23.2	2.54
103	51.6	-0.0996	4.40E-03	0.0996	4.4	23.2	2.31
104	52.1	-0.0896	4.41E-03	0.0896	4.41	23.2	2.08
105	52.6	-0.0796	4.41E-03	0.0796	4.41	23.2	1.85
106	53.1	-0.0696	4.41E-03	0.0696	4.41	23.2	1.62
107	53.6	-0.0596	4.41E-03	0.0596	4.41	23.2	1.39
108	54.1	-0.0496	4.42E-03	0.0496	4.42	23.2	1.15
109	54.6	-0.0396	4.42E-03	0.0396	4.42	23.3	0.922
110	55.1	-0.0296	4.42E-03	0.0296	4.42	23.3	0.689
111	55.6	-0.0196	4.42E-03	0.0196	4.42	23.3	0.457
112	56.1	-0.00956	4.43E-03	0.00956	4.43	23.3	0.223
113	56.6	0.000437	4.43E-03	-0.000437	4.43	23.3	-0.0102
114	56.9	0.000437	4.43E-03	-0.000437	4.43	23.3	-0.0102

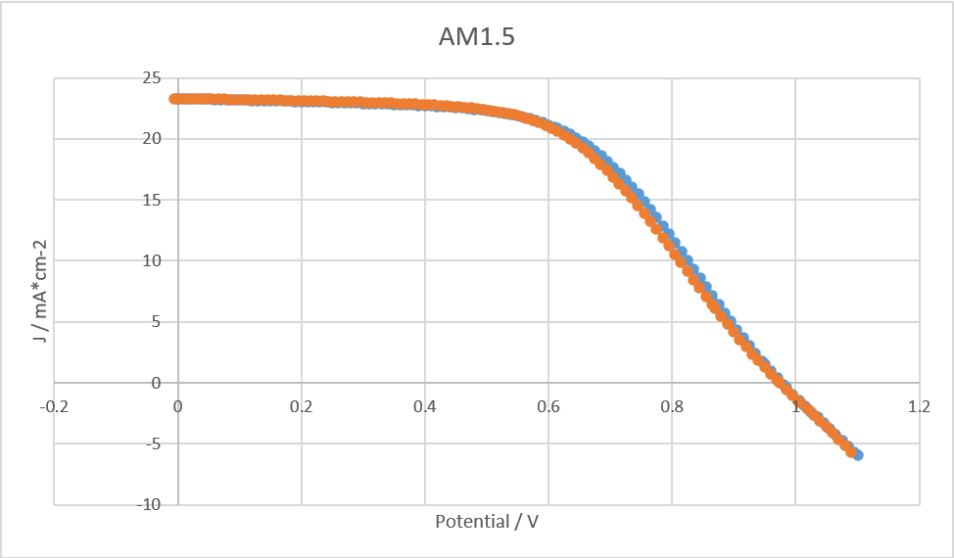

Figure A.1: Example of the J-V curve obtained from the Excel Sheet

$$J\ (\text{mA}\cdot\text{cm}^{-2}) = \frac{I\ (\text{mA})}{A_0(\text{cm}^2)} \tag{A.1}$$

$$P\ (mW \cdot cm^{-2}) = V(V) \times J(\text{mW}\cdot\text{cm}^{-2}) \tag{A.2}$$

Table A.2: Calculated Photovoltaic Parameters obtained from the Excel Files

	Reverse	Forward
Voc	0.975	0.972
Jsc	23.3	23.3
FF	0.569	0.561
Pmax	12.9	12.7
Efficiency	12.9	12.7

$$FF = \frac{P_{máx}\ (\text{mW}\cdot\text{cm}^{-2})}{V_{OC}(\text{V}) \times J_{SC}(\text{mA}\cdot\text{cm}^{-2})} \tag{A.3}$$

$$PCE\ (\%) = \frac{P_{máx}\ (\text{mW}\cdot\text{cm}^{-2})}{P_0\ (\text{mW}\cdot\text{cm}^{-2})} \times 100 \quad \text{(A.4)}$$

A.2 Absorbance Characterization

Table A.3: Example of the Excel Sheet used in the UV-VIS Characterization Performed

Wavelength / nm	Transmittance / %	Reflectance / %	Absorbance / %
200	-0.1	19.9	80.2
201	0	19.7	80.3
202	0	19.4	80.6
203	0.1	19	80.9
204	0	18.6	81.4
205	0.1	18.3	81.6
206	0	18	82
207	0	17.8	82.2
208	0	17.5	82.5
209	0	17.2	82.8
210	0	17	83
211	0	16.7	83.3
212	0	16.4	83.6
213	0	16.2	83.8
214	0	15.9	84.1
215	0	15.7	84.3
216	0	15.4	84.6
217	0	15.2	84.8
218	0	15	85
219	0	14.8	85.2
220	0	14.5	85.5

221	0	14.3	85.7
222	0	14.1	85.9
223	0	13.9	86.1
224	0	13.7	86.3
225	0	13.5	86.5
226	0	13.3	86.7
227	0	13.1	86.9
228	0	12.9	87.1
229	0	12.8	87.2
230	0	12.6	87.4
231	0	12.5	87.5
232	0	12.4	87.6
233	0	12.3	87.7
234	0	12.2	87.8
235	0	12.1	87.9
236	0	12.1	87.9
237	0	12	88
238	0	12	88
239	0	12	88
240	0	12	88
241	0	11.9	88.1
242	0	11.9	88.1
243	0	11.9	88.1
244	0	11.9	88.1
245	0	12	88
246	0	12	88
247	0	12.1	87.9
248	0	12.2	87.8
249	0	12.2	87.8
250	0	12.3	87.7

251	0	12.3	87.7
252	0	12.3	87.7
253	0	12.4	87.6
254	0	12.3	87.7
255	0	12.3	87.7
256	0	12.2	87.8
257	0	12.1	87.9
258	0	12	88
259	0	11.9	88.1
260	0	11.7	88.3
261	0	11.5	88.5
262	0	11.4	88.6
263	0	11.2	88.8
264	0	11	89
265	0	10.9	89.1
266	0	10.7	89.3
267	0	10.6	89.4
268	0	10.5	89.5
269	0	10.4	89.6
270	0	10.3	89.7
271	0	10.2	89.8
272	0	10.1	89.9
273	0	10.1	89.9
274	0	10.1	89.9
275	0	10	90
276	0	10	90
277	0	10	90
278	0	10	90
279	0	10	90
280	0	10	90

281	0	10	90
282	0	10	90
283	0	10.1	89.9
284	0	10.1	89.9
285	0	10.1	89.9
286	0	10.1	89.9
287	0	10.2	89.8
288	0	10.2	89.8
289	0	10.2	89.8
290	0	10.2	89.8
291	0	10.2	89.8
292	0	10.1	89.9
293	0	10.1	89.9
294	0	10.1	89.9
295	0	10	90
296	0	10	90
297	0	10	90
298	0	10	90
299	0	9.9	90.1
300	0	9.9	90.1
301	0	9.8	90.2
302	0	9.7	90.3
303	0	9.6	90.4
304	0	9.5	90.5
305	0	9.4	90.6
306	0	9.2	90.8
307	0	9.1	90.9
308	0	8.9	91.1
309	0	8.8	91.2
310	0	8.7	91.3

311	0	8.6	91.4
312	0	8.6	91.4
313	0	8.5	91.5
314	0	8.5	91.5
315	0	8.5	91.5
316	0	8.4	91.6
317	0	8.4	91.6
318	0	8.4	91.6
319	0	8.4	91.6
320	0	8.3	91.7
321	0	8.3	91.7
322	0	8.2	91.8
323	0	8.2	91.8
324	0	8.1	91.9
325	0	8.1	91.9
326	0	8	92
327	0	8	92
328	0	8	92
329	0	7.9	92.1
330	0	7.9	92.1
331	0	7.9	92.1
332	0	7.9	92.1
333	0	7.8	92.2
334	0	7.8	92.2
335	0	7.8	92.2
336	0	7.8	92.2
337	0	7.8	92.2
338	0	7.7	92.3
339	0	7.7	92.3
340	0	7.7	92.3

341	0	7.6	92.4
342	0	7.6	92.4
343	0	7.6	92.4
344	0	7.5	92.5
345	0	7.5	92.5
346	0	7.5	92.5
347	0	7.4	92.6
348	0	7.4	92.6
349	0	7.4	92.6
350	0	7.4	92.6

$$A(\%) = 100 - [\tau(\%) + R(\%)] \quad \text{(A.5)}$$

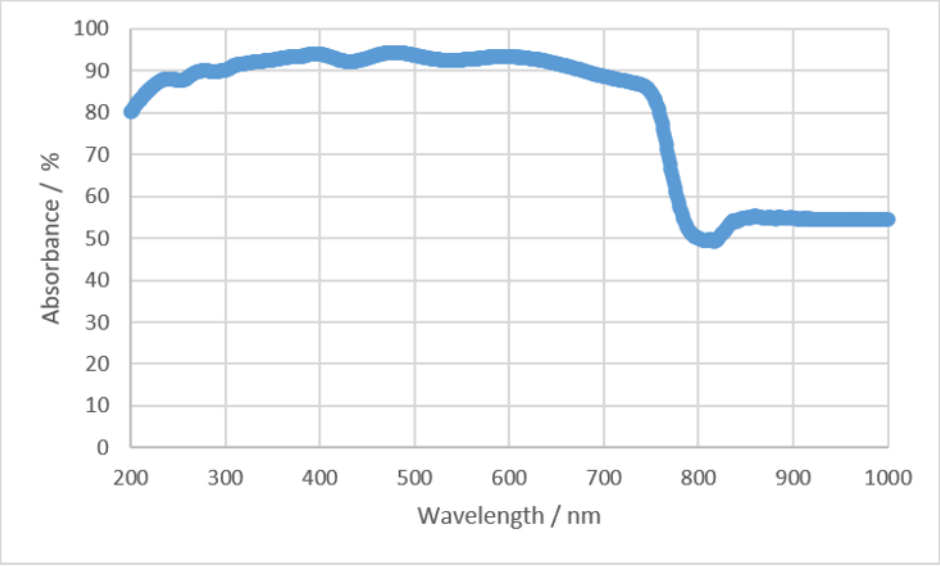

Figure A.2: Absorbance (%) vs Wavelength (nm) Graph

A.3 AM0 to AM1.5 Conversion Script

This appendix details the methodology, governing equations, and underlying assumptions used to convert the terrestrial (AM1.5G) current–voltage (*J–V*) characteristics of the solar

cells measured in this work into their equivalent extraterrestrial (AM0) *J–V* characteristics, using the device's measured external quantum efficiency (EQE) spectrum.

A.3.1. Governing Equations

The incident photon flux at a given wavelength λ is obtained from the spectral irradiance $I(\lambda)$ of the reference solar spectrum (AM1.5G or AM0), where h is the Planck constant and c is the speed of light:

$$\Phi(\lambda)(\text{photons}\cdot\text{s}^{-1}\cdot\text{m}^{-2}\cdot\text{nm}^{-1}) = \frac{I(\lambda)(\text{W}\cdot\text{m}^{-2}\cdot\text{nm}^{-1}) \times \lambda(\text{nm})}{h(\text{J}\cdot\text{s}) \times c(\text{m}\cdot\text{s}^{-1})} \tag{A.6}$$

The short-circuit current density J_{SC} is calculated by integrating the product of the device's $EQE(\lambda)$ and the photon flux $\Phi(\lambda)$ over the measured wavelength range, where e is the elementary charge:

$$J_{SC}(\text{mA}\cdot\text{cm}^{-2}) = e(\text{C}) \int_{\lambda_{\text{min}}}^{\lambda_{\text{max}}} EQE(\lambda)(\%) \cdot \Phi(\lambda)(\text{photons}\cdot\text{s}^{-1}\cdot\text{m}^{-2}\cdot\text{nm}^{-1})\, d\lambda \tag{A.7}$$

Equation (A.7) is evaluated twice using the same EQE(λ) spectrum: once against the AM0 reference spectrum and once against the AM1.5G reference spectrum. This allows us to obtain J_{SC}, AM0 and J_{SC}, AM1.5, respectively. A scale factor k is then defined as the ratio of these two values:

$$k = \frac{J_{sc,AM0}(\text{mA}\cdot\text{cm}^{-2})}{J_{sc,AM1.5}(\text{mA}\cdot\text{cm}^{-2})} \tag{A.8}$$

The AM0-equivalent *J–V* curve is obtained by applying this scale factor uniformly to every current density value of the measured AM1.5G *J–V* curve, at each corresponding voltage V:

$$J_{AM0}(\text{mA}\cdot\text{cm}^{-2}) = k \cdot J_{AM1.5}(\text{mA}\cdot\text{cm}^{-2}) \tag{A.9}$$

From the resulting AM0 *J–V* curve, the FF is calculated from the maximum power point P_{max}, the open-circuit voltage V_{OC}, and the short-circuit current density J_{SC}:

$$FF = \frac{P_{max}(\text{W}\cdot\text{m}^{-2})}{V_{oc}(\text{V}) \cdot J_{sc}(\text{mA}\cdot\text{cm}^{-2})} \tag{A.10}$$

The PCE is calculated from P_{max} and the incident power density of the relevant spectrum, P_{in} (1000 W·m^{-2} for AM1.5G; 1360 W·m^{-2} for AM0):

$$\text{PCE}(\%) = \frac{P_{max}(\text{W}\cdot\text{m}^{-2})}{P_{in}(\text{W}\cdot\text{m}^{-2})} \times 100\% \tag{A.11}$$

A.3.2. Assumptions

The conversion described above relies on the following assumptions:

1 - The device's $EQE(\lambda)$ spectrum is assumed to be identical under AM1.5G and AM0 illumination - i.e., the EQE measured under one standard laboratory light source is treated as intensity - and spectrum - independent and directly applicable to both reference spectra.

2 - The scale factor k, derived purely from the ratio of the two calculated J_{SC} values, is assumed to apply uniformly across the entire J–V curve, not only at the short-circuit point. This implies the shape of the J–V curve (and therefore all recombination and transport mechanisms within the device) is assumed to remain unchanged between the AM1.5G and AM0 spectra, with only its magnitude rescaled.

3 - The open-circuit voltage V_{OC} is assumed to shift consistently with the logarithmic dependence of the diode equation on photocurrent, and this shift is captured implicitly by rescaling J with k rather than being independently recalculated from device physics parameters.

4 - The reference spectra AM1.5G and AM0 used in the calculation (spectral irradiance $I(\lambda)$ as a function of wavelength) are taken as standard tabulated datasets (e.g., ASTM G173-03 for AM1.5G and the ASTM E490 or equivalent for AM0), assumed to accurately represent the terrestrial and extraterrestrial solar spectra, respectively.

5 - The EQE(λ) measurement is assumed to be accurate and sufficiently sampled (in wavelength resolution and range) across the entire spectral response range of the device, such that numerical integration of Equation (A.7) introduces negligible error.

6 - Any spectral mismatch between the EQE measurement's monochromatic probe light and the solar simulator used to record the original AM1.5G J–V curve is assumed to be negligible or already corrected for (i.e., no additional spectral mismatch factor is applied beyond the k scaling).

7 - Series and shunt resistance effects, and any other non-ideal conditions present in the measured AM1.5G J–V curve, are assumed to scale proportionally with the illumination intensity change from AM1.5G to AM0 and are therefore preserved correctly by the uniform current scaling of Equation (A.9).

8 - Device temperature is assumed constant between the AM1.5G measurement and the (hypothetical) AM0 condition, so no temperature-dependent correction is applied to the J–V curve beyond the intensity rescaling.

9 - The incident power densities used for the efficiency calculation (1000 $W \cdot m^{-2}$ for AM1.5G and 1360 $W \cdot m^{-2}$ for AM0) are assumed to be the standard, exact total-integrated-irradiance values of the respective reference spectra.